Archaeomagnetism in Levant and Mesopotamia reveals the largest changes in the geomagnetic field

Ron Shaar[1,1], Yves Gallet[2,2], Yoav Vaknin[1,1], Lilach Gonen[1,1], Mario A.S. Martin[3,3], Israel Finkelstein[3,3], and Matthew Adams[4]

[1]Hebrew University of Jerusalem
[2]Institut De Physique Du Globe De Paris
[3]Tel Aviv University
[4]W.F. Albright Institute of Archaeological Research

November 30, 2022

Abstract

Our understanding of geomagnetic field intensity prior to the era of direct instrumental measurements rely on paleointensity analysis of rocks and archaeological materials that serve as magnetic recorders. Only in rare cases absolute paleointensity datasets are continuous over millennial timescales, provide sub-centennial resolution, and are directly dated using radiocarbon. As a result, fundamental properties of the geomagnetic field, such as its maximum intensity and maximum rate of change have remained a subject of lively discussion. Here, we place firm constraints on these two quantities using Bayesian modelling of well-dated archaeomagnetic intensity data from the Levant and Upper Mesopotamia. We report new data from 23 groups of pottery collected from 18 consecutive radiocarbon-dated archaeological strata from Tel Megiddo, Israel. In the Near East, the period between 1700-550 BCE is now represented by 87 groups of archaeological artifacts, 57 of which dated using radiocarbon and/or direct association to clear historically-dated events, providing an unprecedented sub-century resolution. Moreover, stratigraphic relation between samples collected from multi-layered sited enable further refinement of the archaeomagnetic ages. The Bayesian curve shows four geomagnetic spikes between 1050 and 600 BCE, with virtual axial dipole moment (VADM) reaching values of 155-162 ZAm^2 – much higher than any prediction from geomagnetic field models. Rates of change associated with the four spikes are ˜0.35-0.55 μT/year (˜0.7-1.1 ZAm^2/year) – at least twice the maximum rate inferred from direct observations spanning the past 190 years. Moreover, the increase from 1750 BCE to the first spike depicts the Holocene largest change in field intensity.

Archaeomagnetism in the Levant and Mesopotamia reveals the largest changes in the geomagnetic field

Ron Shaar[1], Yves Gallet[2], Yoav Vaknin[1,3], Lilach Gonen[1], Mario A. S. Martin[3], Matthew J. Adams[4] , Israel Finkelstein[3,5]

[1] The Institute of Earth Sciences, The Hebrew University of Jerusalem, Jerusalem, 91904, Israel

[2] Université Paris Cité, Institut de Physique du Globe de Paris, CNRS, 75005, Paris, France

[3] Institute of Archaeology of Tel Aviv University, Tel Aviv 6997801, Israel

[4] W.F. Albright Institute of Archaeological Research, Jerusalem, Israel

[5] School of Archaeology and Maritime Cultures, University of Haifa, Haifa, Israel

Corresponding author: Ron Shaar (ron.shaar@mail.huji.ac.il)

Key Points:

- Archaeomagnetic intensity data from 23 groups of pottery collected from 18 consecutive radiocarbon-dated strata in Tel Megiddo (Israel).
- The Levantine Archaeomagnetic Curve (LAC): a Bayesian radiocarbon-calibrated archaeointensity curve of the Levant and Mesopotamia.
- Four geomagnetic spikes between 1050–600 BCE define new constraints for maximum field intensity and secular variation rates.

Abstract

Our understanding of geomagnetic field intensity prior to the era of direct instrumental measurements relies on paleointensity analysis of rocks and archaeological materials that serve as magnetic recorders. Only in rare cases absolute paleointensity datasets are continuous over millennial timescales, in sub-centennial resolution, and directly dated using radiocarbon. As a result, fundamental properties of the geomagnetic field, such as its maximal intensity and change rate have remained a subject of lively discussion. Here, we place firm constraints on these two quantities using Bayesian modeling of well-dated archaeomagnetic intensity data from the Levant and Upper Mesopotamia. We report new data from 23 groups of pottery collected from 18 consecutive radiocarbon-dated archaeological strata from Tel Megiddo, Israel. In the Near East, the period of 1700–550 BCE is represented by 84 groups of archaeological artifacts, 55 of which were dated using radiocarbon or a direct link to clear historically-dated events, providing unprecedented sub-century resolution. Moreover, stratigraphic relationships between samples collected from multi-layered sites enable further refinement of the data ages. The Bayesian curve shows four geomagnetic spikes between 1050 and 600 BCE, with virtual axial dipole moment (VADM) reaching values of 155–162 ZAm^2 – much higher than any prediction from geomagnetic field models. Rates of change associated with the four spikes are ~0.35–0.55 μT/year (~0.7–1.1 ZAm^2/year), at least twice the maximum rate inferred from direct observations spanning the past 190 years. The increase from 1750 BCE to 1030 BCE (73 to 161 ZAm^2) depicts the Holocene's largest change in field intensity.

Plain Language Summary

The strength of Earth's magnetic field is changing in an unpredictable manner. Understanding these changes requires precise information on how the field has changed in the past. Direct instrumental measurements of magnetic field intensity began in the 1840s, providing only a short time window into past intensity changes. Here, we explore the more ancient field by analyzing a rare collection of radiocarbon-dated archaeological materials from stratified archaeological settlements and historically-dated burnt structures in the Levant and Mesopotamia. We use new data from Tel Megiddo (Armageddon) to construct a continuous curve of geomagnetic field intensity spanning 2500 years, with unprecedented detail and resolution. The curve depicts the evolution of a high-intensity anomaly, the largest change in intensity observed during the Holocene. Between 1750 and 1050 BCE, the field rapidly increased to values greater than twice those of today, much higher than any prediction derived from available geomagnetic field models. Subsequent oscillations between 1050 and 550 BCE, with extreme peaks, namely 'geomagnetic spikes', reveal change rates of at least twice as fast as the fastest change observed since the advent of direct measurements. Levantine archaeomagnetic data represent a case study in which archaeology provides crucial constraints on the geomagnetic field behavior.

1. Introduction

The absolute intensity of the geomagnetic field was first measured by Carl Friedrich Gauss in 1832 (Courtillot & Le Mouel, 2007). Subsequent measurements with improved precision and spatial resolution have provided quantitative estimates of the amplitude and rate of geomagnetic field intensity changes, but only across the past two centuries. Information from periods preceding observational measurements, fundamental for understanding the magnetic field behavior, is derived from ancient materials that acquired thermoremanent magnetization upon cooling from high temperatures. For the past several millennia, archaeological materials have been the primary source for this information (e.g., Arneitz et al., 2017; Brown et al., 2021), providing most of the data for late Holocene geomagnetic models (Arneitz et al., 2019; Campuzano et al., 2019; Constable et al., 2016; Nilsson et al., 2014; Nilsson et al., 2022; Panovska et al., 2019; Pavon-Carrasco et al., 2014). However, global models are smoothed by design, as they require a tradeoff between model complexity and fit to heterogeneous data. Regional intensity curves provide important insights into field behavior (e.g., Cai et al., 2017; Garcia et al., 2021; Genevey et al., 2016, 2021; Rivero-Montero et al., 2021; Schnepp et al., 2020), but they depend on the quality of the underlying source data. One of the most significant limiting factors for both global and regional field modeling is the limited precision and accuracy of the published ages. Only ~12% of the global published data from the past 10ky data are directly dated with radiocarbon, and in many cases, the exact nature and context of the dated material are not documented. Instead, most archaeomagnetic ages are based on assignment to regional archaeological chronologies, which may have differing interpretations, can be poorly tied to absolute ages, or have large age ranges (e.g., Shaar et al., 2020). Furthermore, unlike paleomagnetic field direction reconstructions, which use stratigraphic constraints in sedimentary sequences to obtain continuous time series, archaeomagnetic intensity datasets are mostly sporadic in time and space. Given the overall uncertainties in the available paleomagnetic and archaeomagnetic data, some of the most fundamental properties of the geomagnetic field, such as its maximum intensity and maximum possible change rate, have remained elusive and the subject of a lively and fruitful debate (Davies & Constable, 2018; Korte & Constable, 2018; Livermore et al., 2014; Livermore et al., 2021).

One way to improve the resolution of archaeomagnetic data is to focus efforts on large multi-layered archaeological sites, which are composed of distinct consecutive strata, and can provide data in stratigraphic order, e.g., Mari (Tell Hariri), Tell Atij and Tell Gudeda in Upper Mesopotamia (Gallet & Butterlin, 2015; Gallet et al., 2020; Gallet et al., 2006; Gallet et al., 2008), Ebla (Tell Mardikh) in Northern Levant (Gallet et al., 2014; Gallet et al., 2008), and Tel Hazor in Southern Levant (Shaar et al., 2020; Shaar et al., 2016). Although these are key sites for Near Eastern archaeology, most of their archaeomagnetic data are not radiocarbon-dated. From this perspective, Tel Megiddo (Israel), with a radiocarbon-based age model covering timespan of 3000-735 BCE time-span, is unique, providing an unprecedented opportunity to construct a stratigraphically constrained radiocarbon-calibrated archaeomagnetic time series.

In the following, we report the data obtained from Tel Megiddo, which to date, is the largest archaeomagnetic intensity dataset available from a single site. We compile the new data with other archaeomagnetic data from the Levant and Mesopotamia that pass our selection criteria. The temporal resolution of the combined data between the 18th and the 6th century BCE is a century or less, as most of the archaeomagnetic ages in this period are derived from radiocarbon-dated contexts and historically-dated burnt structures. Using this high-precision compilation, we develop the Levantine Archaeomagnetic intensity Curve (LAC), utilizing a Bayesian methodology. The LAC elucidates the details of the largest geomagnetic change in the Holocene, associated with the Levantine Iron Age Anomaly (Shaar et al., 2016) and the occurrence of geomagnetic spikes (Ben-Yosef et al., 2009; Shaar et al., 2011; Shaar et al., 2016). We use the LAC to enhance knowledge of the number, duration, and intensity of geomagnetic spikes, which define new robust upper limit constraints for both maximum field intensity and change rate.

2. Archaeomagnetic intensity stratigraphy of Tel Megiddo

2.1. Background

Tel Megiddo (32.585N, 35.185E, Fig. 1) is a world-heritage archaeological site located on the western margins of the Jezreel Valley in northern Israel. Owing to its strategic location on the international route which connected Egypt with Mesopotamia, Megiddo was a central city and an important administrative center throughout the Bronze and Iron Ages (ca. 3500 – 600 BCE). Extensive excavations of the mound have revealed more than thirty Bronze and Iron Age superimposed settlements, with several destruction layers indicating violent endings in military campaigns (Finkelstein, 2009). The chronology of the entire Megiddo sequence was established from Bayesian analyses of ca. 150 radiocarbon samples (the total number of radiocarbon samples at Megiddo is 185) carefully collected from nearly all strata (Boaretto, 2022; Martin et al., 2020; Regev et al., 2014; Toffolo et al., 2014). Special care was taken in assembling the radiocarbon model from mostly short-lived organic materials strongly linked to the archaeological findings. The exceptionally large radiocarbon data from a detailed, continuous, and well-established stratigraphy, along with the intensive ceramic record of Megiddo that defines the relative dating of the region (e.g., late Iron I, early Iron IIA), provides a robust absolute chronology for Near Eastern archaeology.

The archaeomagnetic stratigraphy of Tel Megiddo is based on twenty-three different contexts recovered from 18 layers, excavated in six excavation areas (Fig. 2). Ten contexts (S-3, H-15, K-6, H-11, K-4/H-9/Q-7, Q-4, H-3/Q-2) are destruction layers with distinct boundaries and clear marks of their ending. Megiddo's final destruction by the Assyrian Tiglath-Pileser III is conclusively dated to 732 BCE, based on multiple historical documents. We sampled fragments of indicative pottery from each context, with emphasis on local domestic material. We preferred, when possible, complete or cured vessels that were photographed and documented in the excavation reports. In three contexts (Q-4, Q-5, K-9), we also sampled fragments of cooking ovens (tabuns). The fragments (termed hereafter 'samples' for consistency with previous publications) discussed here include new data, as well as data already published in Shaar et al. (2016) and Shaar et al. (2020), which reported the initial archaeomagnetic stratigraphy of Megiddo. Supplementary Table S1 lists the archaeological details of all the materials analyzed in this study.

2.2. Archaeointensity experiments

Thellier-IZZI-MagIC paleointensity experiments were conducted in the shielded paleomagnetic laboratory at the Institute of Earth Sciences, the Hebrew University of Jerusalem, using two modified ASC TD-48 ovens and a 2G-RAPID superconducting rock magnetometer (SRM). Specimens were prepared by gluing small pieces of pottery inside non-magnetic 22 × 22 × 20 mm square alumina crucibles. The protocol followed the IZZI method (Tauxe & Staudigel, 2004; Yu et al., 2004) with routine pTRM checks at every second temperature step using an oven field of 40, 50, or 60 μT. Heating time ranged from 40 to 65 minutes, depending on the target temperature. In total, each IZZI experiment included 31 or 33 heating steps at 13 or 14 temperature intervals between 100°C to 590°C or 600°C. All specimens were subjected to anisotropy of thermoremanent magnetization (ATRM) experiments, which consisted of eight heating steps at 590°C or 600°C: a baseline zero-field step, six infield steps at orthogonal directions, and an additional alteration check. ATRM alteration parameter was calculated following Shaar et al. (2015) (Table 1). For specimens with ATRM alteration checks > 6%, anisotropy of anhysteretic remanent magnetization (AARM) was measured at a 100mT AC field in 0.1mT DC bias field, at six orthogonal directions, after thermal demagnetization of the specimens. All specimens were subjected to cooling rate correction experiments, which consisted of 4–5 cooling steps from 590 °C or 600 °C to room temperature, following the protocol described in Shaar et al. (2020). Archaeointensity values were calculated with the *Thellier-GUI* program (Shaar & Tauxe, 2013), incorporated into the *PmagPy* software package (Tauxe et al., 2016), using *Thellier Auto Interpreter* algorithm and the acceptance criteria listed in Table 1. Sample results were calculated by averaging at least 3 specimens per sample using the STDEV-OPT algorithm of the *Thellier-GUI* program and the 'extended error bounds' approach (Shaar & Tauxe, 2013; Shaar et al., 2016). When averaging sample data in 'groups' (see section 2.3), we calculated a simple mean of the STDEV-OPT values of the samples. A detailed description of the methods can be found in Shaar et al. (2016) and Shaar et al. (2020). All measurement data are available in the MagIC database (earthref.org/MagIC/19395).

2.3. Results

The archaeomagnetic data from Tel Megiddo, including the data already published in Shaar et al. (2016) and Shaar et al. (2020), include 763 specimens from 175 samples. In this study, we analyze 288 specimens from 85 newly collected samples. In total, 583 specimens and 132 samples pass the criteria listed in Table 1, where archaeointensities obtained at the sample level are calculated from a minimum of 3 specimens. Fig. 3 shows representative cases of a successful specimen and interpretations failing criteria. The importance of the anisotropy and cooling rate corrections is illustrated in Fig. 4. Typically, the bias due to anisotropy and cooling rate effects is 5%–15%; in some cases, the combined corrections exceed 20%. Table S2 (Supplementary Material) lists specimens results, anisotropy and cooling rate correction factors, and values of paleointensity statistics listed in Table 1.

Fig. 5 displays sample data with error bars calculated using the "extended error bounds" approach (Shaar & Tauxe, 2013). In general, samples collected from the same archaeological context (termed hereafter 'group') show good agreement with only two outliers in groups K-4 and Q-4. Levels H-9 and H-3 exhibit a large dispersion of data, with distinctively different values. As the ceramics in each context represent production during a time interval rather than a singular point in time, this probably indicates fast changes in the field during the interval represented in the ceramic assemblage. Thus, we tentatively split the results from these two contexts into two subgroups. The mean archaeointensity of each group is calculated by averaging the sample means. Detailed sample data are provided in Table 2 and Supplementary Table S3. The archaeomagnetic stratigraphy presented in Fig. 5 (Table 2) shows exceptionally large amplitude changes – between ~39 and ~90 μT. In the following sections, we explore in detail this amplitude change depicted in the Megiddo data.

The ages of the groups are based on the Bayesian age model of Megiddo, which is assembled from ~150 radiocarbon samples and takes into account the stratigraphic relationships between strata and correlation between levels excavated at different areas (e.g. Fig. 2a). The published 68.2% and 95.4 % probability age intervals (Boaretto, 2022; Martin et al., 2020; Regev et al., 2014; Toffolo et al., 2014) are shown in Table 2. The actual age ranges we use for the archaeomagnetic analysis overlap the radiocarbon age ranges, but are not identical. This distinction is performed to optimally represent the age range of the ceramic assemblage in each archaeological context, considering the entire archaeological and historical evidence. Thus, the age range of a group may be as short as 50 years for sequences of short-lived phases punctuated by well-dated destruction layers (e.g. Q-4,Q-5,Q-6,Q-7) or 250–300 years for less-constrained strata (e.g. J-4,J-5,J-6).

3. The Levantine Archaeomagnetic Curve (LAC.v.1.0)

The Levantine Archaeomagnetic Curve (LAC) is designed to enable both the statistical analysis of secular variation properties and archaeomagnetic dating. In this article, we focus on the geomagnetic implications of the curve, whereas in a sister article (Vaknin et al., in press), we demonstrate the applications of the curve for correlating ancient historical events. Preliminary versions of the LAC, using an identical methodology as in this study but spanning different time intervals, were published in Shaar et al. (2020) and Gallet et al. (2020). Here, we provide a short description of the different datasets used to construct the LAC and briefly outline the underlying methodology of the Bayesian analysis. A more detailed description of the archaeomagnetic methods, selection criteria, and our approach for sorting and organizing the published data can be found in Shaar et al. (2020). A complete description of the Bayesian method is given in Livermore et al. (2018).

3.1. Data compilation: experimental guidelines

Archaeomagnetic studies in the Levant and Mesopotamia, in the area extending from Egypt in the south to southern Turkey in the north, yielded an incredibly large archaeomagnetic dataset, which includes more than 722 archaeointensity estimates published between 1969 and 2021 and available in the GEOMAGIA50 database (Brown et al., 2015; Brown et al., 2021), the MagIC database (Tauxe et al., 2016), and the ArcheoInt compilation (Genevey et al., 2008). Yet, when these data are simply stacked together, significant discrepancies are evident (Supplementary Material, Fig. S1). From an experimental perspective, screening out the most robust data and assigning a consistent archaeointensity uncertainty to the overall data are not trivial tasks due to large differences in laboratory methods, data analysis approaches, and selection criteria. Moreover, not all of these data were published along with the raw measurement data, preventing a rigorous and identical calculation of the experimental uncertainty. We, therefore, adopt an approach that utilizes only methods that were tested against each other in different laboratories and shown to yield statistically indistinguishable results at the sample level:

- Thellier-IZZI-MagIC: This method incorporates the Thellier-IZZI protocol (Yu et al., 2004) exactly as applied in this study. The automatic interpretation procedure follows the STDEV-OPT algorithm (Shaar & Tauxe, 2013) with the 'LAC criteria' provided in Table 1. All measurement data are available in the MagIC database (https://www.earthref.org/MagIC) and can be re-interpreted using any set of alternative selection criteria.

- Triaxe (Le Goff & Gallet, 2004) or the Triaxe + Coe (Gallet & Le Goff, 2006): The Triaxe method was tested against the Thellier-IZZI-MagIC in a blind test in Shaar et al. (2020) and yielded indistinguishable results. The Triaxe + Coe includes groups of specimens, which were analyzed using both the Thellier-Coe method (Coe et al., 1978) by Genevey et al. (2003) and the Triaxe method by Gallet and Le Goff (2006), and found to be equivalent.

Other data will be included in future LAC compilations if the measurement data can be analyzed using identical procedures and selection criteria as the rest of the LAC data.

Another aspect of the LAC compilation is associated with data hierarchy. A portion of the published archaeomagnetic data was reported as averages of specimens prepared from the same mother sample, while another portion was reported as averages of specimens or samples collected from the same archaeological context. In the LAC compilation, we use the latter approach to avoid over (under)-representation of contexts with more (fewer) samples and to ensure that uncertainties are calculated consistently. Thus, each datum in the LAC compilation represents a 'group', where a group can be, for example, a collection of indicative pottery from a specific stratum, fired mud bricks from a burnt structure, a layer in a slag mound, or storage jars with identical stamp types. The archaeointensity value of a group is calculated as a simple average of the samples' means after screening out outliers (e.g., K-4 and Q-4 in figure 5). Two exceptions to this rule are related to destruction layers: a kiln from Horvat Tevet that had gone out of use when the site had been destroyed (Vaknin et al., in press) and a clay-made floor burnt during the historically-dated Babylonian destruction (Vaknin et al., 2020); in these cases, a large number of specimens collected from the same thermal unit are averaged.

Fig. 6 displays 142 groups between 3000 – 500 BCE passing the experimental criteria. In order to minimize effects related to spatial variability of the field, we constrain the geographic distribution of the data to the region that extends between southern Israel, Cyprus, northern Syria, and eastern Syria (Fig. 1), comprising a circle with a radius of ~500km. Data are displayed in terms of virtual axial dipole moment (VADM) – a transformation from local, latitude-dependent field intensity measurement to the equivalent geomagnetic axial dipole moment. Data from Syria (analyzed using the Triaxe or Triaxe+Coe methods) representing Mesopotamia and northern Levant (Gallet & Al-Maqdissi, 2010; Gallet & Butterlin, 2015; Gallet et al., 2014; Gallet et al., 2020; Gallet et al., 2006; Gallet et al., 2008; Genevey et al., 2003; Livermore et al., 2021), were reported as groups and displayed as published with few minor updates on the ages of some fragment groups (Supplementary Text S4 and the mentioned references for all the data obtained at the specimen/fragment levels). Data from Timna-30 slag mound (Shaar et al., 2011), Tel Hazor (Shaar et al., 2016), and the Judean stamped jars (Ben-Yosef et al., 2017), which were published as samples, are averaged to represent group means (Supplementary Tables S4–S9).

3.2. Data compilation: age estimation guidelines

We distinguish between two sets of data with essentially different approaches for age estimation. The ages of the first set, marked in gray in Fig. 6, were assigned by the excavators of the sites using a complex body of archaeological evidence that does not include absolute radiocarbon ages directly associated with the archaeointensity data. This raises two problems for paleomagnetists and modelers. First, tracing back the considerations used to determine the ages requires specific archaeological expertise, and, therefore, the quality, precision, and robustness of these ages cannot be easily assessed without a detailed description of the age data. Second, in many cases, the archaeological time scales, based on ceramic typology and cultural changes, might be loosely linked to an absolute age scale and may have different age interpretations. Our approach in these cases is to make as few changes as possible to the archaeological ages assigned by the excavators but rather to use wide age range that considers all possible correlations to the absolute age scale.

The ages of the color-coded datasets in Fig. 6 are assigned using radiocarbon or direct associations to historical events whose ages are considered consensuses by most of the archaeological community. The latter are significant for the time interval associated with the Hallstatt Plateau (ca. 800–400 BCE) in the radiocarbon calibration curve (Reimer et al., 2020). From the 8th to 6th century BCE, the ages are based on a correlation to two precisely-dated historical military campaigns described in the Hebrew Bible and other Mesopotamian texts - Assyrian (733–701 BCE) and Babylonian (600 – 586 BCE) – rather than on radiocarbon. In addition, the Aramean occupation (845–815 BCE), which is dated using both radiocarbon and historical constraints, is also used as a useful chronological tie point. The groups with age ranges tied to absolute ages are marked by four different colors in Fig. 6, and include the following datasets:

- The radiocarbon-dated stratigraphy of Tel Megiddo described in this study, which ended in the Assyrian destruction of the city.

- Two radiocarbon-dated layers from Tel Hazor (Stratum XVIII, Stratum XII) and a sequence of three stratigraphically ordered, short-lived phases from strata V-VI that ended in the Assyrian destruction of Hazor (Text S1, Tables S4-S5, supplementary material).

- A radiocarbon-dated sequence of ten slag layers from Timna-30. The Bayesian age model of the mound (Shaar et al., 2011), which was originally established using a magnetostratigraphic correlation with Khirbet en-Nahas (Ben-Yosef et al., 2009), is revised here to include only radiocarbon samples collected from Timna-30 (Text S2, Tables S6-S8, Supplementary Material)

- Materials dated by association to the Assyrian and Babylonian occupations or to the radiocarbon-dated Aramean campaign. This dataset includes 19 burnt structures (Vaknin et al., 2020; Vaknin et al., in press) and three groups of indicative ceramics that can be dated by association with cultural changes related to the occupations. The fired mud-brick structures found in the burnt level are crucial tie points for two reasons. First, as mentioned above, the uncertainty in radiocarbon dating in this period is in the order of 200–400 years due to the plateau in the calibration curve, while the dates of the historical campaigns are unique in their precision. Second, the burnt bricks record a single event, as the fire during the destruction resets their magnetization, in contrast to pottery groups that provide data over a time interval representing a production period.

Supplementary Table S10 lists the VADM and the age range of 142 groups included in the LAC.v.1.0 compilation. We stress that none of the ages in the LAC data compilation were determined or constrained using archaeomagnetism in order to avoid circular reasoning.

3.3. Bayesian modeling

With the data described in Section 3.2 and listed in Supplementary Table S10, we calculate a Bayesian curve with its corresponding 95% credible envelope (Fig. 6, Supplementary Table S11). We term this curve 'Levantine Archaeomagnetic Curve version 1.0', or LAC.v.1.0. The LAC is calculated using the age hyperparameter reverse-jump Monte Carlo Markov Chain (AH-RJMCMC) algorithm developed by Livermore et al. (Livermore et al., 2018) (https://github.com/plivermore/AH-RJMCMC1). The algorithm is based on a piece-wise linear interpolation of the data between vertices drawn in a random-walk-like perturbation within a space allowed by the acceptance criteria. The prior assumptions of the model are: i) the allowed range of vertices' VADM values is set to between 60 and 200 ZAm^2; ii) the allowed number of vertices (K) is between $K_{min} = 1$ and $K_{max} = 150$; iii) ages in all contexts are uniformly distributed, except the ages of Timna, which were modeled as a normal distribution; and iv) group means and standard deviations define a normal distribution of the archaeointensity data. In addition, Supplementary Table S10 defines a stratigraphic order for contexts collected from the multi-layered sites (Tel Megiddo, Tel Hazor, Tell Atij, Tell Gudeda, Timna) and few mutual constraints between groups in Megiddo and Hazor. The AH-RJMCMC procedure takes into account all of these temporal relationships. The model uses the parameters $\sigma_{move} = 30$ yrs, $\sigma_{change} = 10$ Z Am^2, and $\sigma_{birth}=10$ Z Am^2, which define the random perturbation of a vertex in age, in intensity, and that of the linearly interpolated intensity value of a new vertex based on the current vertex distribution respectively. The age of a single datum is perturbed per age-resampling step (num_age_changes = 1); chain length is $2{\cdot}10^8$.

The sub-centennial resolution of the curve from 1100 to 550 BCE (encompassing the Levantine Iron Age anomaly) is achieved through several unique features of the combined datasets. Firstly, we obtained radiocarbon-dated contexts with age uncertainties of approximately a century and, in several cases, even less. Secondly, the stratigraphic relationships in Timna, Megiddo, and Hazor define constraints to the Bayesian model that lead to a reduction in the posterior age ranges. Lastly, we included data obtained from historically well-dated burnt levels and used a dense dataset with a large number of groups during the spike period.

4. Discussion

4.1 New constraints on the highest geomagnetic field intensity

Considering all the published paleointensity estimates from individual samples (i.e., not group means) from the past 5 My available in the GEOMAGIA50 v.3.3 (Brown et al., 2015) and PINT v.8.1.0 (Biggin et al., 2009; Bono et al., 2022) databases, only 1% of the data, which are sporadically scattered in time and space, show VADM > 150 ZAm^2. As such, VADM values calculated from global geomagnetic models do not exceed 140 ZAm^2 (e.g., Arneitz et al., 2019; Constable et al., 2016; Korte & Constable, 2018; Panovska et al., 2019; Pavon-Carrasco et al., 2014). The only exception is the time interval between the end of the 2nd millennium BCE and the middle of the 1st millennium BCE, where a number of archaeomagnetic observations point to high field values (>150 ZAm^2) at several locations: the Levant (Ben-Yosef et al., 2017; Ertepinar et al., 2012; Shaar et al., 2011; Shaar et al., 2016; Vaknin et al., 2020), Caucasus (Shaar et al., 2017), China (Cai et al., 2017), Bulgaria (Kovacheva et al., 2014), Spain (Osete et al., 2020), Canary Islands (Kissel et al., 2015), Azores (Di Chiara et al., 2014) and Hawaii (Pressling et al., 2006). All these observations suggest short duration for the episodes of high intensity values. This behavior is probably associated with a more complex field structure than today's (Korte &

Constable, 2018; Osete et al., 2020; Rivero-Montero et al., 2021) and, presumably, with a local high field anomaly in the Near East, termed the 'Levantine Iron Age Anomaly' (LIAA) (Shaar et al., 2018; Shaar et al., 2017; Shaar et al., 2016).

The highest VADM values during the climax of the LIAA were termed 'geomagnetic spikes' by Ben-Yosef et al. (2009) and Shaar et al. (2011). Note that we use the term 'spike' hereafter in a dual sense: first, to describe a short time interval (about a century long) with rates of intensity change far exceeding those observed in the modern era (1840-2020), which would potentially allow for other spikes to be observed outside of the LIAA, and second, to describe short-lived intensity peaks exceeding the typical values in the geological record. Livermore et al. (2021) questioned the robustness of the spikes and stated that the number of spikes and their values strongly depend on the archaeomagnetic data used, particularly the experimental errors and the averaging scheme adopted (i.e., sample groups versus individual samples). Here, we address the issues raised by Livermore et al. (2021) and assemble a much denser dataset based solely on group averages. This way, each data point in our compilation represents exactly the same quantity and gains the same weight in the Bayesian calculation process. The new curve shows the occurrence of four spikes with peak VADM of 155–162 Z Am^2 around 1030, 840, 740, and 600 BCE. Each spike is represented by several coeval or nearly coeval groups, where overall, fourteen groups have VADM > 150 Z Am^2. Considering that each group represents a time average of several samples, we suggest a value of 155 Z Am^2 as a robust and conservative upper limit for the maximum field value. Yet, based on sample data, higher values may have occurred for short time intervals.

Fig. 7 demonstrates that spike-like values are rare in the paleomagnetic record, showing all the published absolute paleointensity data with ages older than 1500 BCE from the GEOMAGIA50 and PINT databases. Only 49 data points out of 6816 have field values higher than 155 Z Am^2, none of which passes the rather strict statistical tests applied in the LAC. Given the specific conditions associated with the Levantine geomagnetic spikes, the difficulty in detecting similar high-paleointensity values in the global paleointensity record is understandable. First, our dense dataset, including ten archaeointensity groups on average (each consisting of at least two samples) per century during the LIAA interval (Fig. 6a) shows that the duration of the peaks is around a century. Thus, if an average of few samples is required to obtain a robust paleointensity estimate, a large dataset, such as the LAC compilation, is required to detect spikes. Second, global geomagnetic models indicate that the geomagnetic dipole during the LIAA is most likely the highest in the Holocene (Constable et al., 2016; Pavon-Carrasco et al., 2014; Schanner et al., 2022). Thus, the likelihood of detecting spikes may depend on the likelihood that the ancient paleomagnetic dipole was similarly high. Third, the spikes are a regional feature associated with a local geomagnetic anomaly, expressed not only by high field values but also by directional deviations from a dipole field (Osete et al., 2020; Shaar et al., 2018; Shaar et al., 2016). Consequently, there are low chances that the scattered and sparse paleointensity database spanning the geological record can reveal short-lived spikes. Moreover, from the comparison with the global paleointensity database, we can conclude that spikes represent the highest value the geomagnetic field can reach and can serve as a robust upper boundary for the maximum strength of the geomagnetic field at a given location.

4.2 New constraints to maximum secular variation rates

The rates associated with the spikes range between ~0.35 – 0.55 μT/year or 0.7 – 1.1 Z Am^2/year in VADM values (Fig. 6c). To place these values within the context of the global geomagnetic field behavior, we calculate in Fig. 8 the maximum rate in today's field by observing the difference between IGRF models epochs 2015 and 2020 (Alken et al., 2021). For most of Earth's surface, the rates do not exceed 0.1 μT/year (~0.2 Z Am^2/year), and a maximum rate of 0.12 μT/year occurs only in limited areas (Fig. 8a). VADM transformation accounting for the latitudinal dependency of the field yields a maximum rate of 0.25 Z Am^2/year (Fig. 8b). We expand the calculation back to 1840 using the gufm1 model (Jackson et al., 2000) for 1840–1945 and the IGRF models for 1950–2020 (Alken et al., 2021) by looking at the maximum difference in field intensity every five years at any point on Earth's surface. In our calculation we ignored the interval 1945–1950 as we noticed an abrupt and very time-limited change in the rate at few locations, which is likely an artifact caused by problematic global coverage of the data in the 1945 model. The maximum change rate in the past 190 years is not significantly different from today, i.e., 0.18 μT/year or 0.33 Z Am^2/year. These rates are considerably lower than those observed during the time intervals associated with geomagnetic spikes. Hence, LAC.v.1.0 also places new robust constraints on how fast local field intensity can change.

We note that the rates calculated using LAC.v.1.0 appear more moderate than previously considered (Ben-Yosef et al., 2009; Shaar et al., 2011), which had raised questions regarding the dynamo processes behind them (Livermore et al., 2014; Troyano et al., 2020). Although the spikes are now within the range of variations permitted by our current understanding of the geodynamo (Davies & Constable, 2017; Davies & Constable, 2018; Livermore et al., 2014), the fluctuations associated with the spikes remain unprecedented in their amplitude and rate.

4.3. Long-term evolution of the Levantine Iron Age Anomaly

The archeo-magnetostratigraphy of Tel Megiddo reveals the Holocene's greatest amplitude change at multi-century scales between 1750 BCE and 1030 BCE. The increase began with a minimum of 73 Z Am^2 in the 18th century BCE, a period characterized by the lowest intensities in the Near East over the last five millennia, comparable to the low values at the beginning of the 3rd millennium BCE (Fig. 6b). The 700 year-long increase is nearly continuous, punctuated by a century-scale peak around 1500 BCE. The spike period may, therefore, be a climax of a long-term evolution in the geomagnetic field intensity in the Near East, which could result from the occurrence of intense and rapidly evolving flux bundles at the core-mantle boundary. It also contrasts with the period spanning from the 3rd millennium BCE to the 18th century BCE, which shows intensity peaks of moderate amplitudes associated with lower change rates of less than 0.2 μT/year (Figs. 6b,c; see also Gallet et al. (2020)). The significant increase in intensity would then result in spikes instead of intensity peaks, with the first events also being shorter and apparently more frequent, which could reflect a remarkable change in core dynamics.

5. Conclusions

We report here the largest archaeomagnetic intensity dataset currently available from a single site, i.e. Tel Megiddo, with 23 sample groups collected from 18 consecutive radiocarbon-dated archaeological strata.

We assemble a new archaeomagnetic compilation of the Levant and Upper Mesopotamia between 3000 BCE to 550 BCE with 142 different groups of samples. The interval from 1700 BCE to 550 BCE is based mostly on contexts directly dated using radiocarbon and clear associations with well-dated historical military campaigns, providing an unprecedented sub-century resolution. We use this compilation to calculate the Levantine Archaeomagnetic Curve (LAC.v.1.0), a Bayesian regional curve for high-precision archaeomagnetic dating.

The LAC depicts four geomagnetic spikes between 1050 BCE and 600 BCE, each lasting about a century, defining new upper limits on both the maximum local field values and change rate. Considering the overall uncertainty, we suggest 155 ZAm^2 and 0.5 μT/year (1.0 ZAm^2/year in VADM values) as conservative upper boundaries for these quantities.

As a concluding remark, we highlight the challenge in constructing a robust, continuous geomagnetic intensity curve at a sub-centennial resolution over a large millennial time scales. This is made possible in this study by exploiting the advantage of the Near East's abundance of data that allows acquisition of large multiple archaeomagnetic datasets with precise dating, stratigraphic constraints, and cross-correlations between sites. In this respect, Tel Megiddo is an exemplary case study demonstrating a strong link between archaeology, radiocarbon, and geomagnetism.

Acknowledgments

This project has received funding from the European Research Council (ERC) under the European Union's Horizon 2020 research and innovation programme (grant agreement No 804490) to RS. The study was partly supported by the Israel Science Foundation (ISF) grant 1364/15 to RS. It was partly financed by the INSU-CNRS program PNP to YG. Work on the Megiddo samples was supported by the Dan David Foundation and grants from Mark Weissman and Jacques Chahine to IF. We thank Phil Livermore for assisting with the AH-RJMCMC analysis. We thank Maxwell Brown and the anonymous reviewer whose constructive comments helped improve the manuscript.

Open Research

All measurement data are available in the MagIC database (earthref.org/MagIC/19395).

References

Alken, P., Thebault, E., Beggan, C. D., Amit, H., Aubert, J., Baerenzung, J., et al. (2021). International Geomagnetic Reference Field: the thirteenth generation. *Earth Planets and Space, 73*(1) https://doi.org/10.1186/s40623-020-01288-x

Arneitz, P., Egli, R., Leonhardt, R., & Fabian, K. (2019). A Bayesian iterative geomagnetic model with universal data input: Self-consistent spherical harmonic evolution for the geomagnetic field over the last 4000 years. *Physics of the Earth and Planetary Interiors, 290*, 57-75 https://doi.org/10.1016/j.pepi.2019.03.008

Arneitz, P., Leonhardt, R., Schnepp, E., Heilig, B., Mayrhofer, F., Kovacs, P., et al. (2017). The HISTMAG database: combining historical, archaeomagnetic and volcanic data. *Geophysical Journal International, 210*(3), 1347-1359 https://doi.org/10.1093/gji/ggx245
Ben-Yosef, E., Millman, M., Shaar, R., Tauxe, L., & Lipschits, O. (2017). Six centuries of geomagnetic intensity variations recorded by royal Judean stamped jar handles. *Proceedings of the National Academy of Sciences of the United States of America, 114*(9), 2160-2165 https://doi.org/10.1073/pnas.1615797114
Ben-Yosef, E., Tauxe, L., Levy, T. E., Shaar, R., Ron, H., & Najjar, M. (2009). Geomagnetic intensity spike recorded in high resolution slag deposit in Southern Jordan. *Earth and Planetary Science Letters, 287*(3-4), 529-539 https://doi.org/10.1016/j.epsl.2009.09.001
Biggin, A. J., Strik, G. H. M. A., & Langereis, C. G. (2009). The intensity of the geomagnetic field in the late-Archaean: new measurements and an analysis of the updated IAGA palaeointensity database. *Earth Planets and Space, 61*(1), 9-22 https://doi.org/10.1186/Bf03352881
Boaretto, E. (2022). Radiocarbon dating. In M. A. S. Martin & I. Finkelstein (Eds.), *Megiddo VI: The 2010-2014 Seasons*. PA: State College.
Bono, R. K., Paterson, G. A., van der Boon, A., Engbers, Y. A., Grappone, J. M., Handford, B., et al. (2022). The PINT database: a definitive compilation of absolute palaeomagnetic intensity determinations since 4 billion years ago. *Geophysical Journal International, 229*(1), 522-545 https://doi.org/10.1093/gji/ggab490
Brown, M. C., Donadini, F., Korte, M., Nilsson, A., Korhonen, K., Lodge, A., et al. (2015). GEOMAGIA50.v3: 1. general structure and modifications to the archeological and volcanic database. *Earth Planets and Space, 67*, 1-31 https://doi.org/10.1186/s40623-015-0232-0
Brown, M. C., Herve, G., Korte, M., & Genevey, A. (2021). Global archaeomagnetic data: The state of the art and future challenges. *Physics of the Earth and Planetary Interiors, 318* https://doi.org/10.1016/j.pepi.2021.106766
Cai, S. H., Jin, G. Y., Tauxe, L. S., Deng, C. L., Qin, H. F., Pan, Y. X., & Zhu, R. X. (2017). Archaeointensity results spanning the past 6 kiloyears from eastern China and implications for extreme behaviors of the geomagnetic field. *Proceedings of the National Academy of Sciences of the United States of America, 114*(1), 39-44 https://doi.org/10.1073/pnas.1616976114
Campuzano, S. A., Gomez-Paccard, M., Pavon-Carrasco, F. J., & Osete, M. L. (2019). Emergence and evolution of the South Atlantic Anomaly revealed by the new paleomagnetic reconstruction SHAWQ2k. *Earth and Planetary Science Letters, 512*, 17-26 https://doi.org/10.1016/j.epsl.2019.01.050
Coe, R., Gromme, S., & Mankinen, E. (1978). Geomagnetic paleointensities from radiocarbon-dated lava flows on Hawaii and question of Pacific nondipole low. *Journal of Geophysical Research*, 1740-1756 https://doi.org/10.1029/JB083iB04p01740
Constable, C., Korte, M., & Panovska, S. (2016). Persistent high paleosecular variation activity in southern hemisphere for at least 10 000 years. *Earth and Planetary Science Letters, 453*, 78-86 https://doi.org/10.1016/j.epsl.2016.08.015
Courtillot, V., & Le Mouel, J. L. (2007). The study of earth's magnetism (1269-1950): A foundation by peregrinus and subsequent development of geomagnetism and paleomagnetism. *Reviews of Geophysics, 45*(3) https://doi.org/10.1029/2006rg000198
Davies, C., & Constable, C. (2017). Geomagnetic spikes on the core-mantle boundary. *Nature Communications, 8* https://doi.org/10.1038/ncomms15593
Davies, C. J., & Constable, C. G. (2018). Searching for geomagnetic spikes in numerical dynamo simulations. *Earth and Planetary Science Letters, 504*, 72-83 https://doi.org/10.1016/j.epsl.2018.09.037
Di Chiara, A., Tauxe, L., & Speranza, F. (2014). Paleointensity determination from Sao Miguel (Azores Archipelago) over the last 3 ka. *Physics of the Earth and Planetary Interiors, 234*, 1-13 https://doi.org/10.1016/j.pepi.2014.06.008

Ertepinar, P., Langereis, C. G., Biggin, A. J., Frangipane, M., Matney, T., Okse, T., & Engin, A. (2012). Archaeomagnetic study of five mounds from Upper Mesopotamia between 2500 and 700 BCE: Further evidence for an extremely strong geomagnetic field ca. 3000 years ago. *Earth and Planetary Science Letters, 357*, 84-98 https://doi.org/10.1016/j.epsl.2012.08.039

Finkelstein, I. (2009). Destructions: Megiddo as a case study. In J. D. Schloen (Ed.), *Exploring the Longue Durée* (pp. 113-126). Indiana: Eisenbrauns.

Gallet, Y., & Al-Maqdissi, M. (2010). Archeomagnetism in Mishirfeh-Qatna: New data on the evolution of intensity in the earthly magnetic field in the Middle East during the last millenia. *Akkadica, 131*(1), 29-46

Gallet, Y., & Butterlin, P. (2015). Archaeological and geomagnetic implications of new archaeomagnetic intensity data from the Early Bronze High Terrace "Massif Rouge' at Mari (Tell Hariri, Syria). *Archaeometry, 57*, 263-276 https://doi.org/10.1111/arcm.12112

Gallet, Y., D'Andrea, M., Genevey, A., Pinnock, F., Le Goff, M., & Matthiae, P. (2014). Archaeomagnetism at Ebla (Tell Mardikh, Syria). New data on geomagnetic field intensity variations in the Near East during the Bronze Age. *Journal of Archaeological Science, 42*, 295-304 https://doi.org/10.1016/j.epsl.2017.11.013

Gallet, Y., Fortin, M., Fournier, A., Le Goff, M., & Livermore, P. (2020). Analysis of geomagnetic field intensity variations in Mesopotamia during the third millennium BC with archeological implications. *Earth and Planetary Science Letters, 537* https://doi.org/10.1016/j.epsl.2020.116183

Gallet, Y., Genevey, A., Le Goff, M., Fluteau, F., & Ali Eshraghi, S. (2006). Possible impact of the Earth's magnetic field on the history of ancient civilizations. *Earth and Planetary Science Letters, 246*(1-2), 17-26 https://doi.org/10.1016/j.epsl.2006.04.001

Gallet, Y., & Le Goff, M. (2006). High-temperature archeointensity measurements from Mesopotamia. *Earth and Planetary Science Letters, 241*(1-2), 159-173 https://doi.org/10.1016/j.epsl.2005.09.058

Gallet, Y., Le Goff, M., Genevey, A., Margueron, J., & Matthiae, P. (2008). Geomagnetic field intensity behavior in the Middle East between similar to 3000 BC and similar to 1500 BC. *Geophysical Research Letters, 35*(2) https://doi.org/10.1029/2007gl031991

Garcia, R., Perez-Rodriguez, N., Goguitchaichvili, A., Ceja, M. R., Morales, J., Soler, A. M., & Urrutia-Fucugauchi, J. (2021). On the absolute geomagnetic intensity fluctuations in Mexico over the last three millennia. *Journal of South American Earth Sciences, 106* https://doi.org/ARTN 102927
10.1016/j.jsames.2020.102927

Genevey, A., Gallet, Y., Thebault, E., Livermore, P. W., Fournier, A., Jesset, S., et al. (2021). Archeomagnetic intensity investigations of French medieval ceramic workshops: Contribution to regional field modeling and archeointensity-based dating. *Physics of the Earth and Planetary Interiors, 318*

Genevey, A., Gallet, Y., Constable, C. G., Korte, M., & Hulot, G. (2008). ArcheoInt: An upgraded compilation of geomagnetic field intensity data for the past ten millennia and its application to the recovery of the past dipole moment. *Geochemistry Geophysics Geosystems, 9* https://doi.org/Artn Q04038
10.1029/2007gc001881

Genevey, A., Gallet, Y., Jesset, S., Thebault, E., Bouillon, J., Lefevre, A., & Le Goff, M. (2016). New archeointensity data from French Early Medieval pottery production (6th-10th century AD). Tracing 1500 years of geomagnetic field intensity variations in Western Europe. *Physics of the Earth and Planetary Interiors, 257*, 205-219

Genevey, A. S., Gallet, Y., & Margueron, J. C. (2003). Eight thousand years of geomagnetic field intensity variations in the eastern Mediterranean. *Journal of Geophysical Research-Solid Earth, 108*(B5) https://doi.org/10.1029/2001jb001612

Jackson, A., Jonkers, A. R. T., & Walker, M. R. (2000). Four centuries of geomagnetic secular variation from historical records. *Philosophical Transactions of the Royal Society of London Series a-*

Mathematical Physical and Engineering Sciences, 358(1768), 957-990 https://doi.org/10.1098/rsta.2000.0569

Kirschvink, J. L. (1980). The Least-Squares Line and Plane and the Analysis of Paleomagnetic Data. *Geophysical Journal of the Royal Astronomical Society, 62*(3), 699-718 https://doi.org/10.1111/j.1365-246X.1980.tb02601.x

Kissel, C., Laj, C., Rodriguez-Gonzalez, A., Perez-Torrado, F., Carracedo, J. C., & Wandres, C. (2015). Holocene geomagnetic field intensity variations: Contribution from the low latitude Canary Islands site. *Earth and Planetary Science Letters, 430*, 178-190 https://doi.org/10.1016/j.epsl.2015.08.005

Korte, M., & Constable, C. G. (2018). Archeomagnetic Intensity Spikes: Global or Regional Geomagnetic Field Features? *Frontiers in Earth Science, 6* https://doi.org/10.3389/feart.2018.00017

Kovacheva, M., Kostadinova-Avramova, M., Jordanova, N., Lanos, P., & Boyadzhiev, Y. (2014). Extended and revised archaeomagnetic database and secular variation curves from Bulgaria for the last eight millennia. *Physics of the Earth and Planetary Interiors, 236*, 79-94

Le Goff, M., & Gallet, Y. (2004). A new three-axis vibrating sample magnetometer for continuous high-temperature magnetization measurements: applications to paleo- and archeo-intensity determinations. *Earth and Planetary Science Letters, 229*(1-2), 31-43 https://doi.org/10.1016/j.epsl.2004.10.025

Livermore, P. W., Fournier, A., & Gallet, Y. (2014). Core-flow constraints on extreme archeomagnetic intensity changes. *Earth and Planetary Science Letters, 387*, 145-156 https://doi.org/10.1016/j.epsl.2013.11.020

Livermore, P. W., Fournier, A., Gallet, Y., & Bodin, T. (2018). Transdimensional inference of archeomagnetic intensity change. *Geophysical Journal International, 215*(3), 2008-2034 https://doi.org/10.1093/gji/ggy383

Livermore, P. W., Gallet, Y., & Fournier, A. (2021). Archeomagnetic intensity variations during the era of geomagnetic spikes in the Levant. *Physics of the Earth and Planetary Interiors, 312* https://doi.org/10.1016/j.pepi.2021.106657

Martin, M. A. S., Finkelstein, I., & Piasetzky, E. (2020). Radiocarbon-dating the Late Bronze Age: Cultural and historical considerations on Megiddo and beyond. *Bulltin of the American Schools of Oriental Research, 384* https://doi.org/10.1086/709576

Nilsson, A., Holme, R., Korte, M., Suttie, N., & Hill, M. (2014). Reconstructing Holocene geomagnetic field variation: new methods, models and implications. *Geophysical Journal International, 198*(1), 229-248 https://doi.org/10.1093/gji/ggu120

Nilsson, A., Suttie, N., Stoner, J. S., & Muscheler, R. (2022). Recurrent ancient geomagnetic field anomalies shed light on future evolution of the South Atlantic Anomaly. *Proceedings of the National Academy of Sciences, 119*(24), e2200749119 https://doi.org/doi:10.1073/pnas.2200749119

Osete, M. L., Molina-Cardin, A., Campuzano, S. A., Aguilella-Arzo, G., Barrachina-Ibanez, A., Falomir-Granell, F., et al. (2020). Two archaeomagnetic intensity maxima and rapid directional variation rates during the Early Iron Age observed at Iberian coordinates. Implications on the evolution of the Levantine Iron Age Anomaly. *Earth and Planetary Science Letters, 533* https://doi.org/10.1016/j.epsl.2019.116047

Panovska, S., Korte, M., & Constable, C. G. (2019). One hundred thousand years of geomagnetic field evolution. *Reviews of Geophysics, 57*(4), 1289-1337 https://doi.org/10.1029/2019rg000656

Paterson, G. A., Tauxe, L., Biggin, A. J., Shaar, R., & Jonestrask, L. C. (2014). On improving the selection of Thellier-type paleointensity data. *Geochemistry Geophysics Geosystems, 15*(4), 1180-1192 https://doi.org/10.1002/2013gc005135

Pavon-Carrasco, F. J., Osete, M. L., Torta, J. M., & De Santis, A. (2014). A geomagnetic field model for the Holocene based on archaeomagnetic and lava flow data. *Earth and Planetary Science Letters, 388*, 98-109 https://doi.org/10.1016/j.epsl.2013.11.046

Pressling, N., Laj, C., Kissel, C., Champion, D., & Gubbins, D. (2006). Palaeomagnetic intensities from C-14-dated lava flows on the Big Island, Hawaii: 0-21 kyr. *Earth and Planetary Science Letters, 247*(1-2), 26-40 https://doi.org/10.1016/j.epsl.2006.04.026

Regev, J., Finkelstein, I., Adams, M. J., & E., B. (2014). Wiggled-matched 14C chronology of Early Bronze Megiddo and the synchronization of Egyptian and Levantine chronologies. *Egypt and the Levant 24*, 241-264

Reimer, P. J., Austin, W. E. N., Bard, E., Bayliss, A., Blackwell, P. G., Ramsey, C. B., et al. (2020). The Intcal20 Northern hemisphere radiocarbon age calibration curve (0-55 Cal Kbp). *Radiocarbon, 62*(4), 725-757 https://doi.org/10.1017/Rdc.2020.41

Rivero-Montero, M., Gomez-Paccard, M., Pavon-Carrasco, F. J., Cau-Ontiveros, M. A., Fantuzzi, L., Martin-Hernandez, F., et al. (2021). Refining geomagnetic field intensity changes in Europe between 200 CE and 1800 CE. New data from the Mediterranean region. *Physics of the Earth and Planetary Interiors, 317* https://doi.org/ARTN 106749
10.1016/j.pepi.2021.106749

Schanner, M., Korte, M., & Holschneider, M. (2022). ArchKalmag14k: A Kalman-Filter Based Global Geomagnetic Model for the Holocene. *Journal of Geophysical Research-Solid Earth, 127*(2) https://doi.org/10.1029/2021JB023166

Schnepp, E., Thallner, D., Arneitz, P., & Leonhardt, R. (2020). New archeomagnetic secular variation data from Central Europe, II: Intensities. *Physics of the Earth and Planetary Interiors, 309* https://doi.org/ARTN 106605
10.1016/j.pepi.2020.106605

Selkin, P. A., & Tauxe, L. (2000). Long-term variations in palaeointensity. *Philosophical Transactions of the Royal Society a-Mathematical Physical and Engineering Sciences, 358*(1768), 1065-1088 https://doi.org/10.1098/rsta.2000.0574

Shaar, R., Bechar, S., Finkelstein, I., Gallet, Y., Martin, M. A. S., Ebert, Y., et al. (2020). Synchronizing Geomagnetic Field Intensity Records in the Levant Between the 23rd and 15th Centuries BCE: Chronological and Methodological Implications. *Geochemistry Geophysics Geosystems, 21*(12) https://doi.org/10.1029/2020GC009251

Shaar, R., Ben-Yosef, E., Ron, H., Tauxe, L., Agnon, A., & Kessel, R. (2011). Geomagnetic field intensity: How high can it get? How fast can it change? Constraints from Iron Age copper slag. *Earth and Planetary Science Letters, 301*(1-2), 297-306 https://doi.org/10.1016/j.epsl.2010.11.013

Shaar, R., Hassul, E., Raphael, K., Ebert, Y., Segal, Y., Eden, I., et al. (2018). The first catalog of archaeomagnetic directions from Israel with 4,000 years of geomagnetic secular variations. *Frontiers in Earth Science, 6* https://doi.org/10.3389/feart.2018.00164

Shaar, R., & Tauxe, L. (2013). Thellier GUI: An integrated tool for analyzing paleointensity data from Thellier-type experiments. *Geochemistry Geophysics Geosystems, 14*(3), 677-692 https://doi.org/10.1002/ggge.20062

Shaar, R., Tauxe, L., Ben-Yosef, E., Kassianidou, V., Lorentzen, B., Feinberg, J. M., & Levy, T. E. (2015). Decadal-scale variations in geomagnetic field intensity from ancient Cypriot slag mounds. *Geochemistry Geophysics Geosystems, 16*(1), 195-214 https://doi.org/10.1002/2014gc005455

Shaar, R., Tauxe, L., Goguitchaichvili, A., Devidze, M., & Licheli, V. (2017). Further evidence of the Levantine Iron Age geomagnetic anomaly from Georgian pottery. *Geophysical Research Letters, 44*(5), 2229-2236 https://doi.org/10.1002/2016gl071494

Shaar, R., Tauxe, L., Ron, H., Ebert, Y., Zuckerman, S., Finkelstein, I., & Agnon, A. (2016). Large geomagnetic field anomalies revealed in Bronze to Iron Age archeomagnetic data from Tel Megiddo and Tel Hazor, Israel. *Earth and Planetary Science Letters, 442*, 173-185 https://doi.org/10.1016/j.epsl.2016.02.038

Tauxe, L., Shaar, R., Jonestrask, L., Swanson-Hysell, N. L., Minnett, R., Koppers, A. A. P., et al. (2016). PmagPy: Software package for paleomagnetic data analysis and a bridge to the Magnetics

Information Consortium (MagIC) Database. *Geochemistry Geophysics Geosystems, 17*(6), 2450-2463 https://doi.org/10.1002/2016gc006307
Tauxe, L., & Staudigel, H. (2004). Strength of the geomagnetic field in the Cretaceous Normal Superchron: New data from submarine basaltic glass of the Troodos Ophiolite. *Geochemistry Geophysics Geosystems, 5* https://doi.org/10.1029/2003GC000635
Toffolo, M. B., Arie, E., Martin, M. A. S., Boaretto, E., & Finkelstein, I. (2014). Absolute chronology of Megiddo, Israel, in the Late Bronze and Iron Ages: High-resolution radiocarbon dating. *Radiocarbon, 56*(1), 221-244 https://doi.org/10.2458/56.16899
Troyano, M., Fournier, A., Gallet, Y., & Finlay, C. C. (2020). Imprint of magnetic flux expulsion at the core-mantle boundary on geomagnetic field intensity variations. *Geophysical Journal International, 221*(3), 1984-2009 https://doi.org/10.1093/gji/ggaa126
Vaknin, Y., Shaar, R., Gadot, Y., Shalev, Y., Lipschits, O., & Ben-Yosef, E. (2020). The Earth's magnetic field in Jerusalem during the Babylonian destruction: A unique reference for field behavior and an anchor for archaeomagnetic dating. *Plos One, 15*(8) https://doi.org/10.1371/journal.pone.0237029
Vaknin, Y., Shaar, R., Lipschits, O., Mazar, A., Maeir, A., Garfinkel, Y., et al. (in press). Reconstructing biblical military campaigns using geomagnetic field data *Proceedings of the National Academy of Sciences*
Yu, Y. J., Tauxe, L., & Genevey, A. (2004). Toward an optimal geomagnetic field intensity determination technique. *Geochemistry Geophysics Geosystems, 5* https://doi.org/10.1029/2003gc000630

Table 1: Acceptance criteria, LAC.v.1.0

Criteria group *	Statistic	Threshold value	Description	Reference †
Specimen	FRAC	0.79	Fraction parameter	Shaar and Tauxe (2013)
	B	0.1	Scatter parameter	Coe et al. (1978); Selkin and Tauxe (2000)
	SCAT	True	Scatter parameter	Shaar and Tauxe (2013)
	GAP-MAX	0.5	Maximum gap	Shaar and Tauxe (2013)
	N_{PTRM}	2	Number of pTRM checks	
	N	5	Number of data points	
	MAD	5	Maximum Angular Deviation of the zero field steps	Kirschvink (1980)
	DANG	10	Deviation Angle	Tauxe and Staudigel (2004)
	Alteration check (correction)	6%	Alteration check in TRM anisotropy and cooling rate experiments	Shaar et al. (2015)
Sample (pottery vessel, furnace, brick, slag)	N_{min}	3	Number of specimens	
	$N_{min\_aniso\_corr}$	at least half of the specimens	Minimum number of specimens with anisotropy correction	
	$N_{min\_cr\_corr}$	1	Minimum number of specimens with cooling rate correction	
	Σ	$\sigma <$ 3 μT OR σ % < 8%	Standard deviation of the sample mean	
	Anisotropy sample test	6%	If the mean anisotropy correction of all the specimens from the same sample (fragment) is higher than this value, specimens without anisotropy correction are discarded	

* For a complete description and definitions of paleointensity statistics, see Paterson et al. (2014).

Table 2: Archaeointensity results in Tel Megiddo.

Megiddo Group	**Name in LAC.v.1.0***	**Published radiocarbon age range 68.2% probability interval (95.4 % probability interval) (BCE)†**	**Age range in LAC.v.1.0 compilation (BCE) ‡**	**N samples**	**n specimens**	**B (μT)**	**B σ (μT)**	**VADM (ZAm^2)**	**VADM σ (ZAm^2)**
Q-2	mgq02	801-756 (805-735); Assyrian destruction level	820-732	4	15	74.6	3.6	140.3	6.9
H-3-low	mgh03-low	-	820-732	7	37	76.7	3.7	144.3	6.9
H-3-high	mgh03-high			4	18	89.6	2.7	168.6	5.1
Q-4	mgq04	897-821 (901-809)	890-840	3	14	76.4	1.7	143.7	3.1
Q-5	mgq05	956-894 (967-848)	925-875	6	30	69	3.8	129.8	7.1
H-7	Mgh07	930-900 (945-860)	925-875	3	16	71.8	3.7	135.1	6.9
Q-6	mgq06	979-911 (989-876)	950-900	4	16	64.6	3.2	121.5	6
Q-7	mgq07	1047-975 (1052-946)	1050-950	6	18	71	2.7	133.5	5.1
H-9-low	mgh09-low	1038-976 (1056-936)	1050-950	3	15	69.1	4	129.9	7.5
H-9-high	mgh09-high			2	9	83.2	0.4	156.5	0.7
K-4	mgk04	1037-951 (1053-908)	1050-950	4	15	75.5	4.9	142	9.1
H-10	mgh10	1068-1031 (1087-1023)	1100-1025	5	15	69.7	4.3	131	8.1
H-11	mgh11	1105-1051 (1115-1041)	1125-1075	10	30	69.7	4.8	131.1	9.1
K-6	mgk06	1148-1123 (1168-1104)	1175-1125	7	31	64.2	2.6	120.8	4.9
K-8	mgk08	1238-1178 (1268-1158)	1250-1175	8	33	57.3	3.2	107.8	6
K-9	mgk09	1323-1230 (1381-1201)	1400-1250	6	20	54.2	2.2	102	4.1

F-10	mgf10	1545-1354 (1561-1313)	1550-1400	3	14	50.6	1.3	95.2	2.5
H-15	mgh15	1557-1509 (1572-1463)	1550-1475	5	25	54.9	4.3	103.3	8
K-10	mgk10	1581-1545 (1596-1535)	1600-1550	8	35	52.2	5.7	98.2	10.7
K-11	mgk11	1626-1579 (1643-1561)	1650-1600	4	21	52.2	4.5	98.2	8.4
F-13	mgf13	-	1900-1700	4	25	42	2.5	78.9	4.6
S-3	mgs03	1942-1902 (1965-1886)	1950-1900	4	12	38.8	3.5	72.9	6.6
J-6	mgj06	2860-2540 (2880-2450)	2850-2500	4	15	39	0.9	73.4	1.8
J-5	mgj05	2920-2720 (2970-2670)	2900-2800	4	12	44.2	4.3	83.2	8
J-4 §	mgj04	3060-2880 (3180-2830)	3100-2900	8	46	41.1	7.1	77.3	13.3
J-4a §	mgj04a	3060-2880 (3180-2830)	3100-2900	3	10	40.1	1.6	75.4	3.1

* Name in model data (Supplementary Table S10)

† Radiocarbon data from Regev et al. (2014); Toffolo et al. (2014)**;** Martin et al. (2020); Boaretto (2022); There are no radiocarbon data from H-03, and the age is linked to the Assyrian destruction level. Ages from S-3 are preliminary. There are no radiocarbon data from F-13, and the age is inferred from correlation to strata in areas K and S.

‡ Age range used in the archaeomagnetic compilation and in Bayesian modelling.

§ J-4 and J-4a are two groups from the same level. J-4a fragments were collected from loci representing the final days of the temple, whereas the J-4 items originated from a fill context.

Figure 1: Map showing Tel Megiddo and other sites in the Levant and Western Upper Mesopotamia used to construct the Levantine Archaeomagnetic Curve (LAC.v.1.0) shown in Fig. 6. Color code is as in Fig. 6.

Figure 2: Tel Megiddo. a) Aerial photo of the mound displaying the excavation areas discussed in the text. b) Tel Megiddo stratigraphy showing all the contexts analyzed for archaeointensity. The shaded cells mark destruction layers.

Figure 3: Representative results of specimen analysis conducted in this study. (a–d) Red (blue) circles, and triangles in the main Arai plots are ZI steps, IZ steps, and pTRM checks, respectively. Heating temperatures (C°) are displayed near the symbols. Blue (red) squares in the inset Zijderveld plots are x-y (x-z) projections of the remaining NRMs, where the x-axis is rotated to the direction of the NRM. The green line is the best fit. a) Specimen passing all criteria. b–d) Interpretations failing the SCAT (b), FRAC (c), and MAD+DANG (d) criteria. e) A successful cooling rate experiment. Blue circles are four measurements at three different cooling rates, and the red square is a projection of the ancient cooling rate on the best-fit (dashed line).

Figure 4: Histograms of anisotropy and cooling rate corrections.

Figure 5: Archaeomagnetic stratigraphy of Tel Megiddo constructed from 132 samples. Full circles (red squares) represent the archaeointensity of samples (group means). Number of samples used to calculate the group means is indicated above each error bar. Vertical lines represent chrono-stratigraphic division. Fragment (sample) groups are plotted according to their relative age.

Figure 6: An archaeointensity curve. a, b) Levantine Archaeomagnetic Intensity Curve (LAC.v.1.0). Colored symbols are groups of samples directly dated with radiocarbon or by clear association with dated historical events. Gray symbols represent groups dated using various archaeological methods. From the 17^{th} to the 6^{th} centuries, there is at least one directly-dated context per century. Curve and shaded area in (a–b) are the average and the 95% credible interval calculated using the AH-RJMCMC algorithm (Livermore et al., 2018), respectively. c) Rate of change. Dashed red and dotted orange lines show the maximum rate for 1840–2020 and the maximum rate in today's field (Fig. 7), respectively. The oscillation pattern revealed in (a) includes four spikes with VADM >150 ZAm^2 and a change rate of 0.35–0.55 µT/year (0.7–1.1 ZAm^2) (c).

Figure 7: Comparison of spikes' paleointensity with the global databases. a) PINT v.8.1.0 database (Bono et al., 2022). b) GEOMAGIA50 v.3.3 (Brown et al., 2015) before 3500 yBP. Horizontal lines show the value of 155 ZAm^2 corresponding to the spike with the lowest intensity maximum according to LAC.v.1.0 (Fig. 6). N is the number of paleointensity estimates below and above 155 ZAm^2.

Figure 8: Maximum change rate of the geomagnetic field intensity for 1840-2020. a-b) Intensity and VADM rate of change in toady's field, calculated using the IGRF13 model (Alken et al., 2021) epochs 2015-2020. c-d) Maximum intensity and VADM rate of change for 1840-2020, calculated using the IGRF models (Alken et al., 2021) between 1950-2020 and the gufm1 model (Jackson et al., 2000) between 1840-1950. e) Field intensity and rate of change at the location

with the maximum B change (40°S, 45°E). f) VADM and rate of change at the location with the maximum VADM change (20°N, 65°W).

Figure 1.

a)

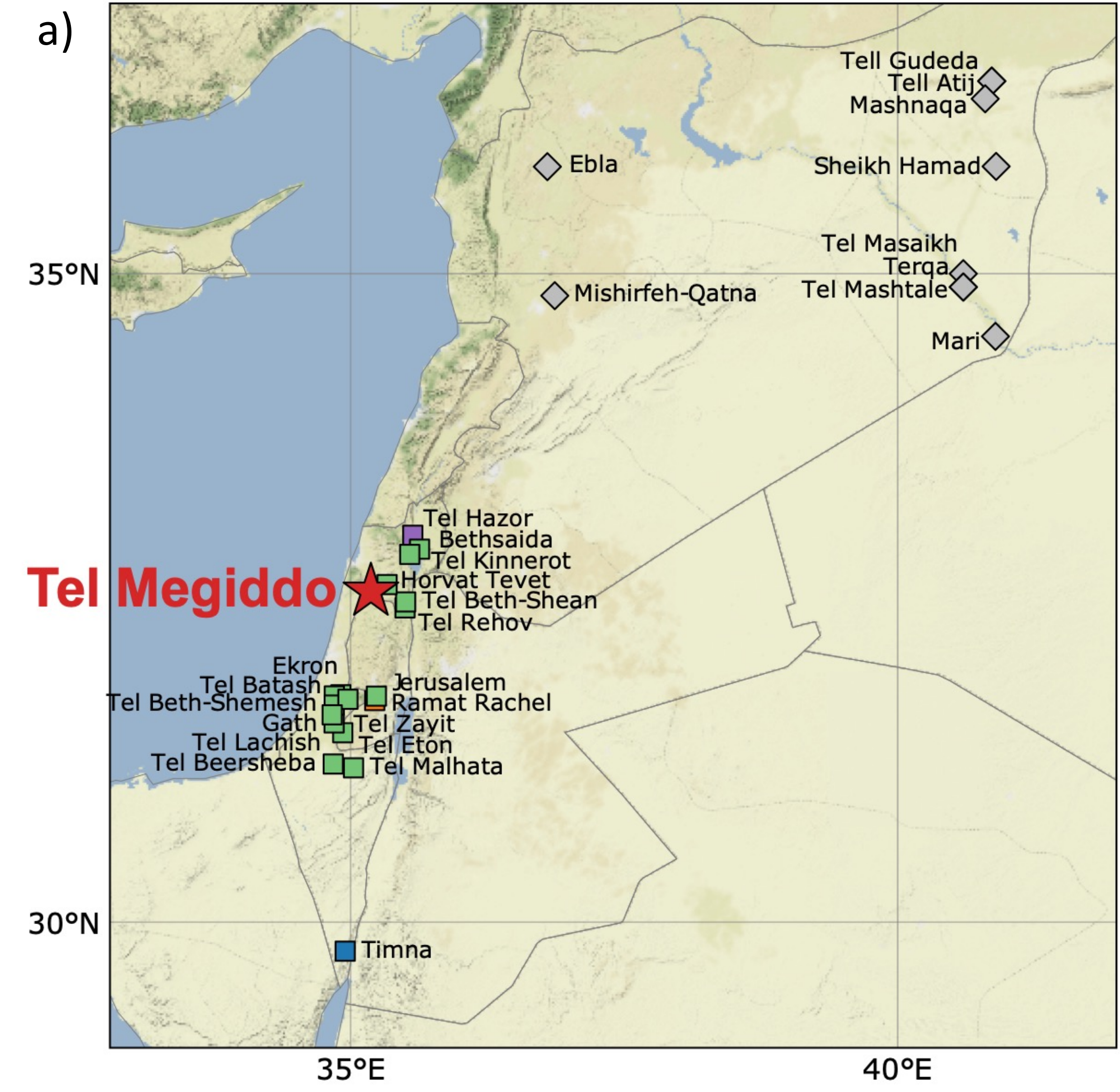
Tell Gudeda
Tell Atij
Mashnaqa
Ebla
Sheikh Hamad
Tel Masaikh
Terqa
Tel Mashtale
Mishirfeh-Qatna
Mari
35°N
Tel Hazor
Bethsaida
Tel Kinnerot
Tel Megiddo
Horvat Tevet
Tel Beth-Shean
Tel Rehov
Ekron
Tel Batash
Tel Beth-Shemesh
Gath
Tel Lachish
Tel Beersheba
Jerusalem
Ramat Rachel
Tel Zayit
Tel Eton
Tel Malhata
30°N
Timna
35°E
40°E

Figure 2.

a)

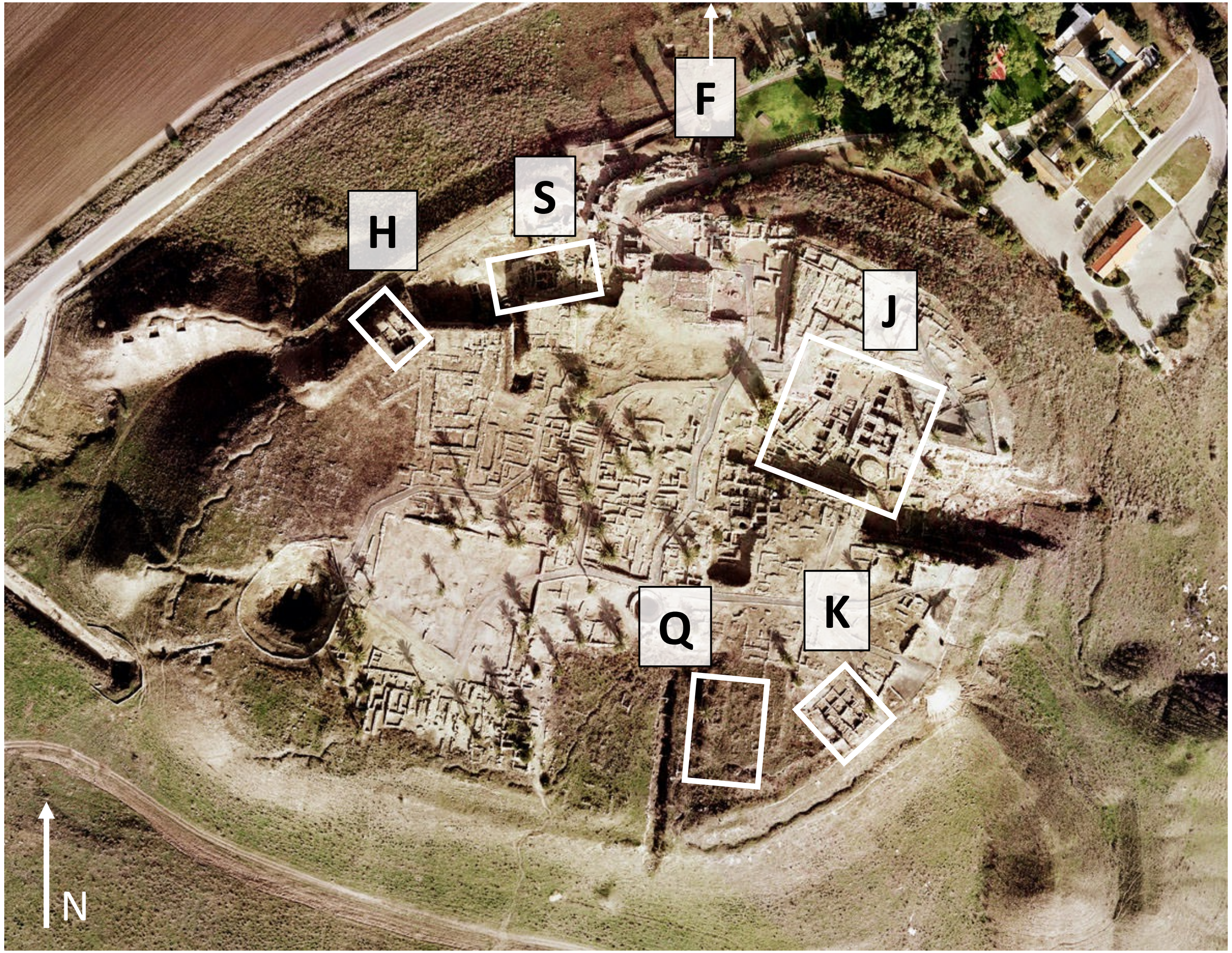

b)

Area / Period	J	S	F	K	H	Q
Early Iron IIB					H-3	Q-2
Late Iron IIA						Q-4
Middle Iron IIA					H-7	Q-5
Early Iron IIA						Q-6
Late Iron I				K-4	H-9	Q-7
Middle Iron I					H-10	
Early Iron I					H-11	
Late Bronze III				K-6		
Late Bronze IIB				K-8		
Late Bronze IIA-IIB				K-9		
Late Bronze I			F-10		H-15	
Middle Bronze III				K-10		
Middle Bronze III				K-11		
Middle Bronze II			F-13			
Middle Bronze I		S-3				
Early Bronze III	J-6					
Early Bronze III	J-5					
Early Bronze IB	J-4					

Figure 3.

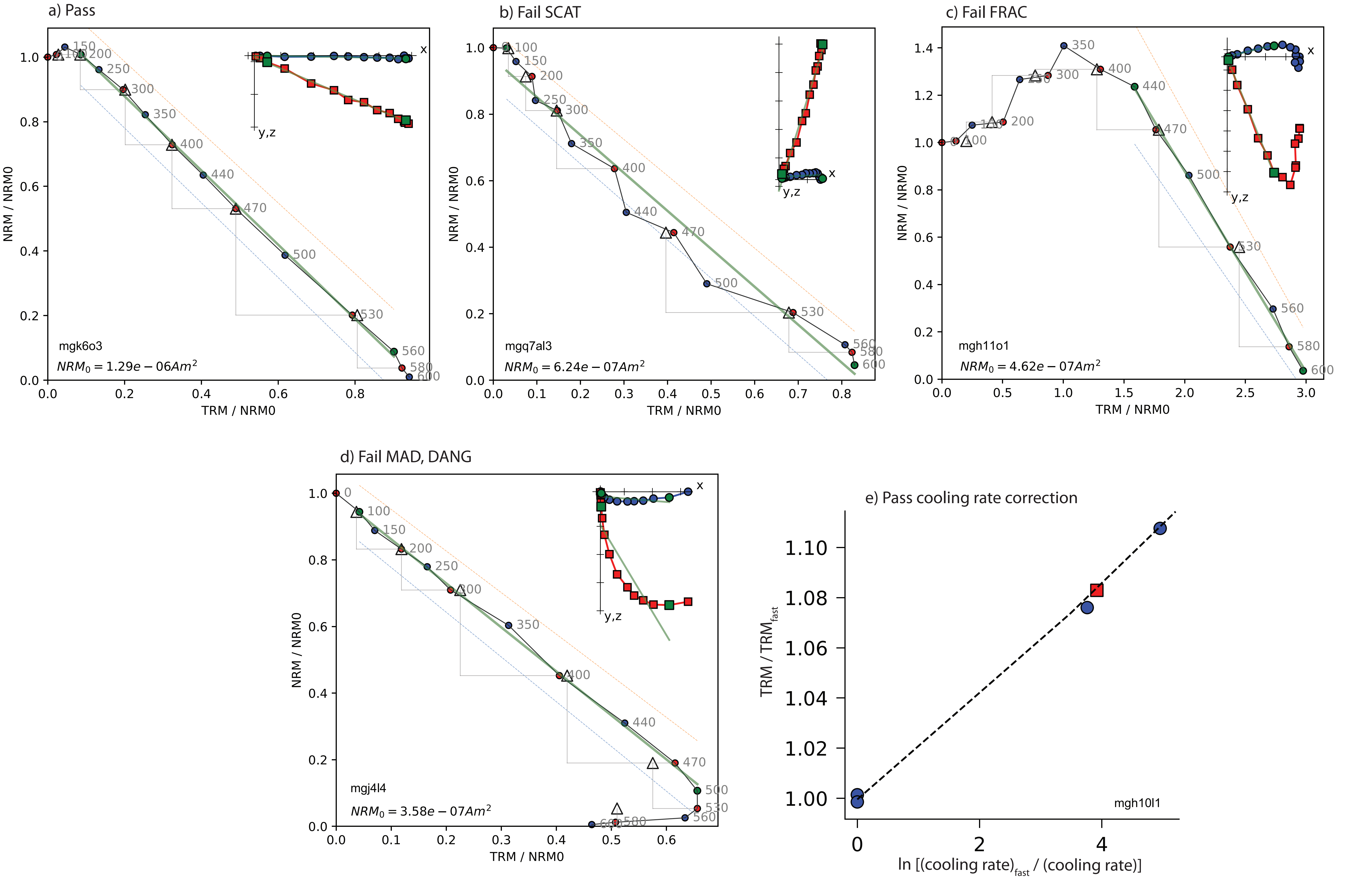

a) Pass
mgk6o3
$NRM_0 = 1.29e-06Am^2$
b) Fail SCAT
mgq7al3
$NRM_0 = 6.24e-07Am^2$
c) Fail FRAC
mgh11o1
$NRM_0 = 4.62e-07Am^2$
d) Fail MAD, DANG
mgj4l4
$NRM_0 = 3.58e-07Am^2$
NRM / NRM0
TRM / NRM0
e) Pass cooling rate correction
mgh10l1
TRM / TRM_{fast}
ln [(cooling rate)$_{fast}$ / (cooling rate)]

Figure 4.

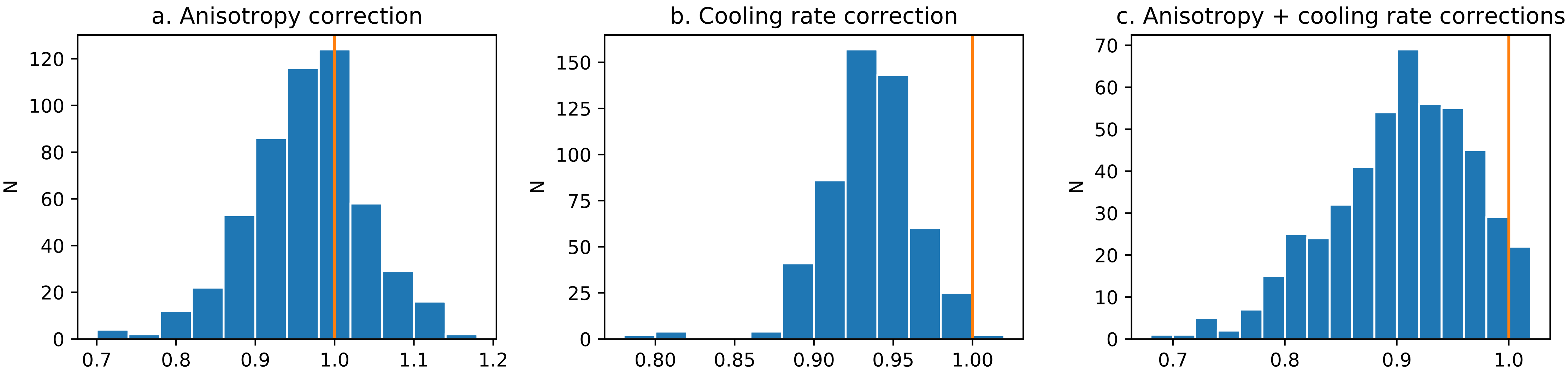
a. Anisotropy correction
b. Cooling rate correction
c. Anisotropy + cooling rate corrections
N
0
20
40
60
80
100
120
0.7
0.8
0.9
1.0
1.1
1.2
0
25
50
75
100
125
150
0.80
0.85
0.90
0.95
1.00
0
10
20
30
40
50
60
70

Figure 5.

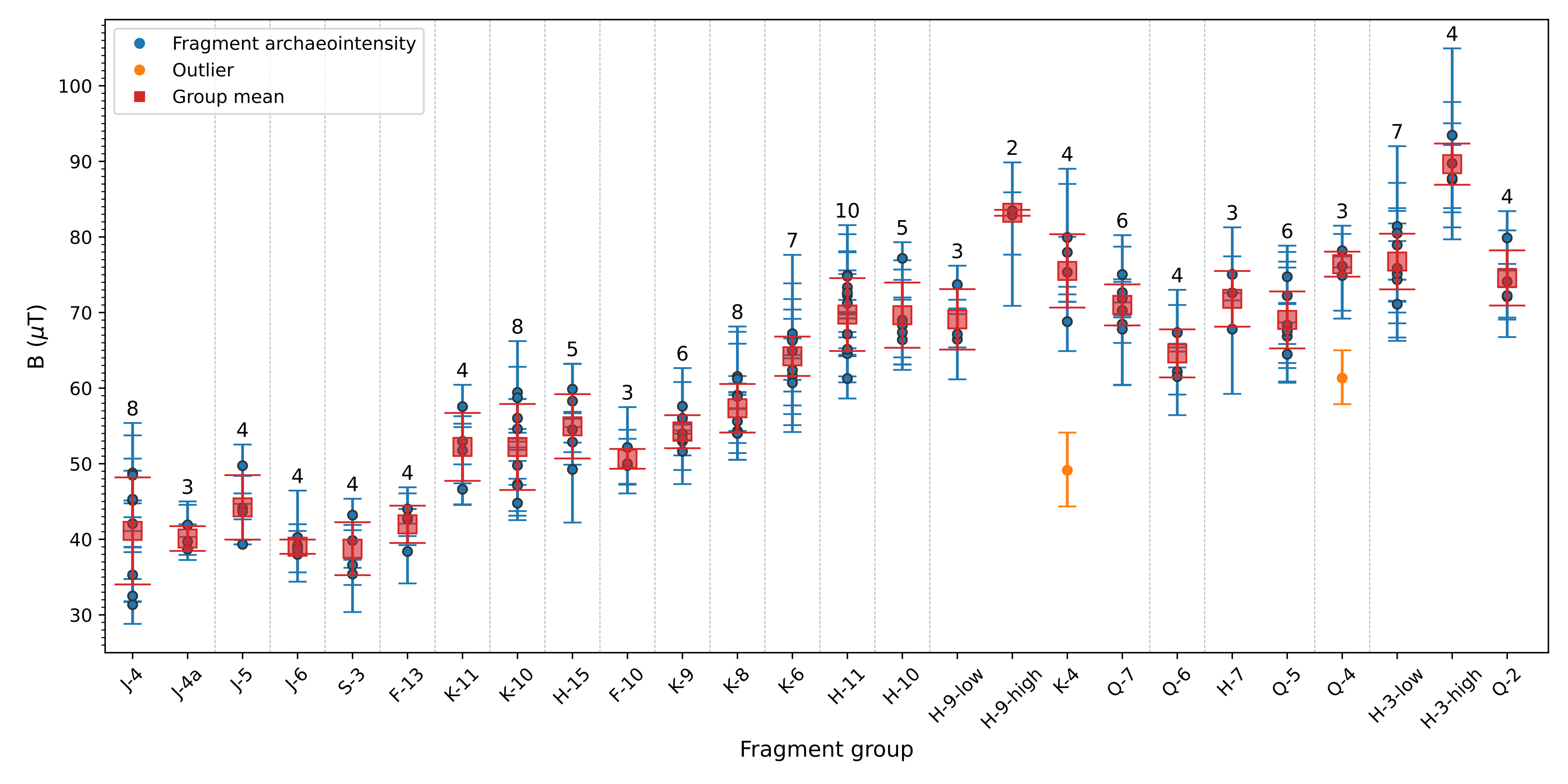

Fragment archaeointensity
Outlier
Group mean
B (μT)
Fragment group
J-4
J-4a
J-5
J-6
S-3
F-13
K-11
K-10
H-15
F-10
K-9
K-8
K-6
H-11
H-10
H-9-low
H-9-high
K-4
Q-7
Q-6
H-7
Q-5
Q-4
H-3-low
H-3-high
Q-2

Figure 6.

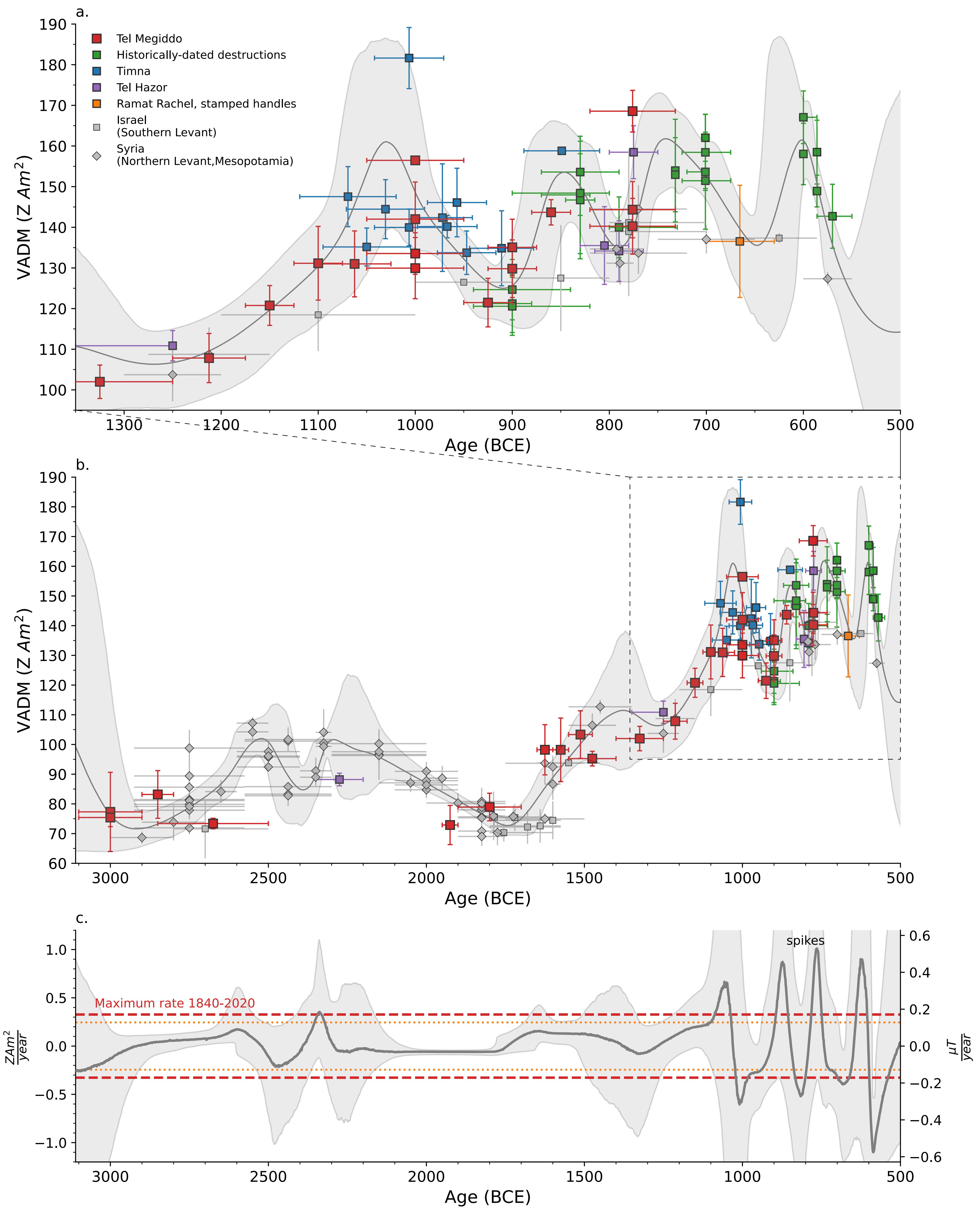
a.
Tel Megiddo
Historically-dated destructions
Timna
Tel Hazor
Ramat Rachel, stamped handles
Israel
(Southern Levant)
Syria
(Northern Levant,Mesopotamia)
VADM (Z Am^2)
Age (BCE)
b.
VADM (Z Am^2)
Age (BCE)
c.
Maximum rate 1840-2020
spikes
$\frac{ZAm^2}{year}$
$\frac{\mu T}{year}$
Age (BCE)

Figure 7.

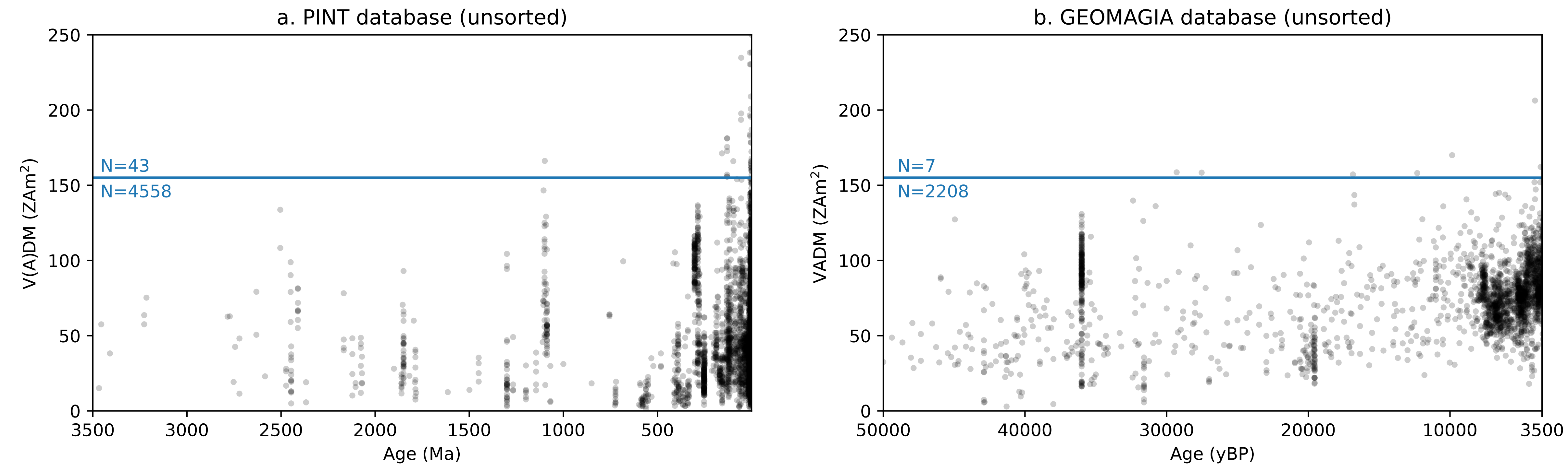

a. PINT database (unsorted)
N=43
N=4558
V(A)DM (ZAm^2)
Age (Ma)
250
200
150
100
50
0
3500
3000
2500
2000
1500
1000
500
b. GEOMAGIA database (unsorted)
N=7
N=2208
VADM (ZAm^2)
Age (yBP)
50000
40000
30000
20000
10000
3500

Figure 8.

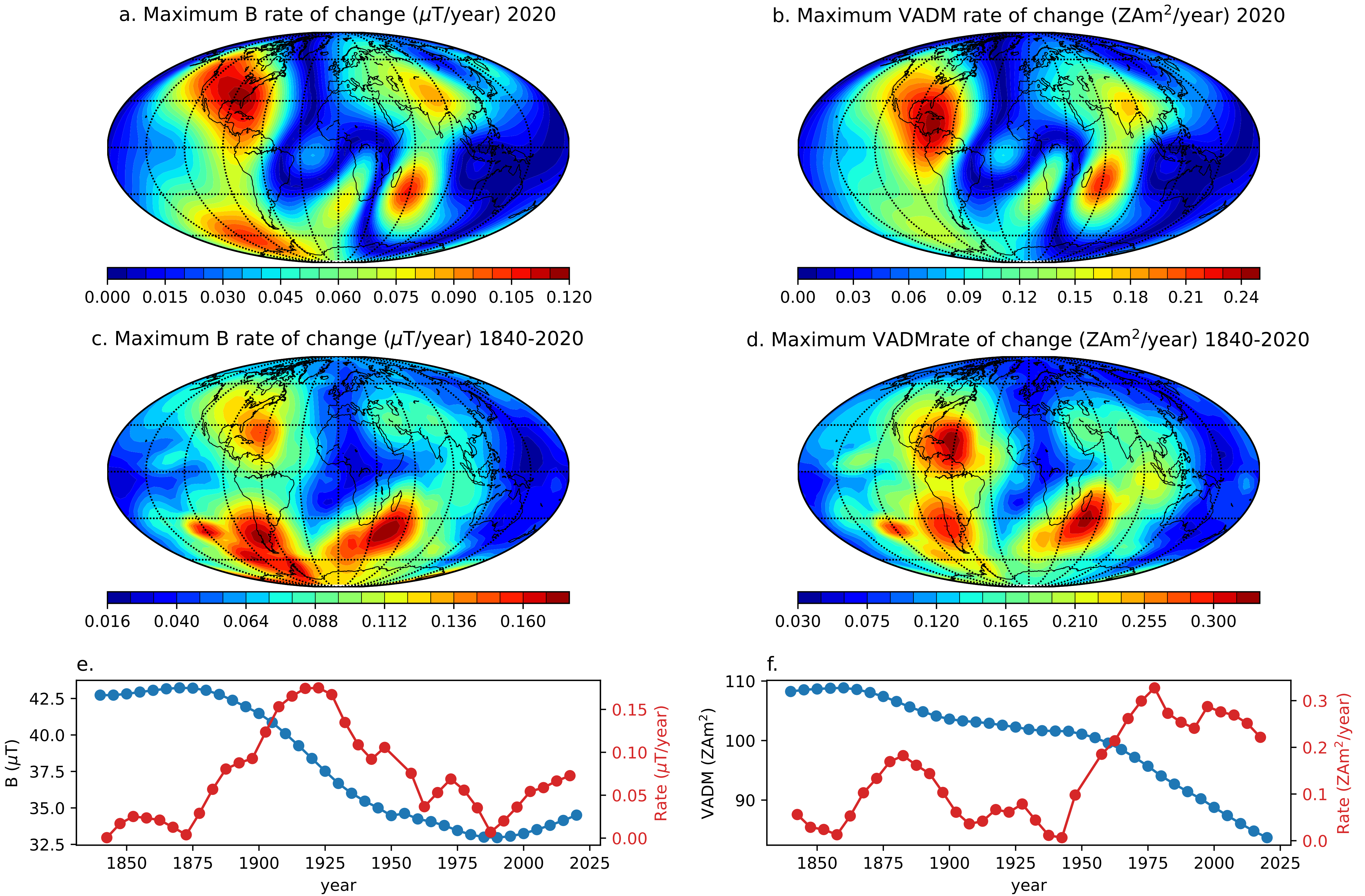
a. Maximum B rate of change (μT/year) 2020
0.000 0.015 0.030 0.045 0.060 0.075 0.090 0.105 0.120
b. Maximum VADM rate of change (ZAm2/year) 2020
0.00 0.03 0.06 0.09 0.12 0.15 0.18 0.21 0.24
c. Maximum B rate of change (μT/year) 1840-2020
0.016 0.040 0.064 0.088 0.112 0.136 0.160
d. Maximum VADMrate of change (ZAm2/year) 1840-2020
0.030 0.075 0.120 0.165 0.210 0.255 0.300
e.
B (μT)
Rate (μT/year)
year
f.
VADM (ZAm2)
Rate (ZAm2/year)
year

JGR

Supporting Information for

Archaeomagnetism in the Levant and Mesopotamia reveals the largest changes in the geomagnetic field

Ron Shaar[1], Yves Gallet[2], Yoav Vaknin[1,3], Lilach Gonen[1], Mario A. S. Martin[3], Matthew J. Adams[4] , Israel Finkelstein[3,5]

[1] The Institute of Earth Sciences, The Hebrew University of Jerusalem, Jerusalem, 91904, Israel

[2] Université Paris Cité, Institut de Physique du Globe de Paris, CNRS, 75005, Paris, France

[3] Institute of Archaeology of Tel Aviv University, Tel Aviv 6997801, Israel

[4] W.F. Albright Institute of Archaeological Research, Jerusalem, Israel

[5] School of Archaeology and Maritime Cultures, University of Haifa, Haifa, Israel

Contents of this file

Additional Supporting Information (Files uploaded separately)

Introduction

This supporting information file includes additional text and tables associated with re-analysis of published data: an update on the archaeological ages and new divisions of the previously published samples to 'groups',

- Tel Hazor: Text S1, Tables S4-S5

- Timna-30: Text S2, Tables S6-S8
- Stamped Judean jars: Text S3, Tables S9
- Syrian fragment groups: Text S4

Text S1. Revisions and updates to published archaeomagnetic data from Tel Hazor

Tel Hazor archaeointensity results are similar to those published in Shaar et al. (2016). Yet, in Shaar et al. (2016) we did not divide the data from strata V-VI to phases. Here, we split strata V-VI to three distinct groups according to the corresponding archaeological phases. The three phases are stratigraphically ordered within one excavation area and end in the historically-dated Assyrian destruction of Tel-Hazor (the same destruction of Tel Megiddo). Therefore, these contexts are treated in the model as firm historically-constrained ages (colored symbols in Fig. 6 main text). The ages of the groups are shown in Table S3. Table S4 shows the published archaeointensity data from Tel Hazor calculated as group means.

Text S2. Revisions and updates to published archaeomagnetic data from Timna-30

The original data from Shaar et al. (2011) were re-interpreted in Shaar et al. (2016) using the same interpretation method and selection criteria used here and in Shaar et al. (2020); Shaar et al. (2016). Here, these samples are grouped according to slag layers. All layers, except layer 0 consist of at least three samples. The data in layer 6 is clustered in two sub-groups of samples: one group with two samples that have paleointensity > 90 μT, and a second group with three samples that have paleointensity < 80 μT. The groups means are given in Table S5.

The age model of Timna-30 slag mound was originally based on magnetostratigraphic correlation with radiocarbon ages of Khirbet en-Nahas (KEN) (Ben-Yosef et al., 2009; Levy et al., 2008). However, the archaeointensity analysis in KEN did not follow all the procedures, which have become standard in later studies, and as a result, almost all slag samples from KEN fail the selection criteria used in LAC.v.1.0. We therefore revert to the age model of Timna-30 that uses the five radiocarbon dates from Timna-30 slag mound only (Fig. S1 and Table S1 in Shaar et al., 2011, supplementary material). As the published ages in Shaar et al. (2011) were calibrated using an older radiocarbon calibration curve, we recalibrate them here using the latest IntCal20 (Reimer et al., 2020) (Table S6). Bayesian age model was calculated with Oxcal program using "Sequence" command to account for the stratigraphic constraints. The ages of the slag layers from which the organic samples were collected (i.e. layer "8", Fig. 3 in Shaar et al., 2011) are the modeled ages shown in Table S7. The ages of the other layers (ten slag layers and nine sterile layers between the slag layers) are extrapolated evenly between the dated layers and shown in Table S8.

Text S3. Revisions and updates to Judean stamped handles data

Data of Judean stamped handles from Ben-Yosef et al. (2017) and Vaknin et al. (submitted) are grouped following Vaknin et al. (submitted). The groups data are given in Table S8.

Text S4. Revisions and updates to Judean stamped handles data

The ages of the following groups of pottery fragments previously published in Gallet et al. (2006) and Genevey et al. (2003) have been updated to take into account more recent findings (Masetti-Rouault, 2016):

- The age of group Lot 05 is updated to 1275-1150
- The age of group TM01 is updated to 803-775
- The age of group Lot 28 is updated to 820-765
- The age of group Lot 29 is updated to 750-650

In addition,

- The age of group SY46 from Ebla is updated to 2300-2000 BCE to be consistent with other groups from close contexts (SY53-SY54-SY55)

The ages of the results obtained from Tell Atij and Tell Gudeda (Gallet et al., 2020) are updated to 2750 +/- 175 BCE and 2437.5 +/- 137.5 BCE, respectively, and further constrained by their time-order relationship. This option allows us to consider no a priori on the accumulation rates across the two archaeological sequences (see Gallet et al. (2020) for details)

Stratum/Phase	Samples	New age range
Hazor-V-B (hz05-B)	hz05a,hz05,hz05d,hz05	-800, -750
Hazor-V-C (hz05-C)	hz05b,hz05e,hz05g,hz05h	-815, -765
Hazor-VI (hz06)	hz06a, hz06b, hz06c	-830, -780

Table S4. Archaeointensity grouping of strata Hazor V-VI.

Group name	Stratum	N fragments	n specimens	B (μT)	B σ (μT)	VADM (ZAm^2)	VADM σ (ZAm^2)	Age	Age σ
hz20	Hazor XX	4	16	38.1	5.3	71.6	9.9	-2650	150
hz18 *	Hazor XVIII	3	12	46.9	1.1	88.2	2.1	-2275	75
HZ17F	Hazor XVII-F	4	15	39.8	2.5	74.8	4.6	-1785	100
HZ17E	Hazor XVII-E	3	13	37.5	1.7	70.5	3.3	-1755	100
HZ17D	Hazor XVII-D	3	15	39.8	2.5	74.9	4.8	-1720	100
HZ16C	Hazor XVI-C	4	16	38.1	3.3	71.7	6.1	-1680	112.5
HZ16B	Hazor XVI-B	4	16	39.2	3.5	73.7	6.6	-1640	112.5
HZ16A	Hazor XVI-A	4	17	39.7	4.1	74.7	7.7	-1600	112.5
hz15	Hazor XV	3	9	49.9	0.5	93.8	1	-1550	100
hz13 †	Hazor XIII	4	21	58	2.5	109.1	4.7	-1250	50
hz11	Hazor XI	3	10	63	4.8	118.5	8.9	-1100	100
hz10	Hazor X	2	8	67.3	0.4	126.5	0.7	-950	50
hz07	Hazor VII	5	23	67.8	6.9	127.5	13	-850	50
hz06	Hazor VI	3	15	72.1	5.1	135.5	9.6	-805	25
hz05-C	Hazor V-C	4	23	71.3	4	134.2	7.5	-790	25
hz05-B	Hazor V-B	3	15	84.3	3.5	158.5	6.5	-775	25

* Based on unpublished radiocarbon ages
† Age based on radiocarbon data (Lev et al., 2021)

Table S5. Tel Hazor archaeointensity groups data used in LAC.v.1.0.

Layer	Group name	N fragments	n specimens	B (μT)	B σ (μT)	VADM (ZAm^2)	VADM σ (ZAm^2)
9	Timna30-09	3	13	75.2	3.8	147.5	7.4
8	Timna30-08	3	12	68.9	2.4	135.2	4.7
7	Timna30-07	4	18	73.7	3.7	144.5	7.3
6	Timna30-06-spikes	2	8	92.6	3.8	181.6	7.5
6	Timna30-06	3	14	71.4	2.3	140	4.5
5	Timna30-05	4	18	72.6	6.7	142.4	13.2
4	Timna30-04	3	9	71.5	1.4	140.2	2.8
3	Timna30-03	3	12	74.5	4.3	146.1	8.4
2	Timna30-02	3	16	68.2	2.7	133.7	5.3
1	Timna30-01	4	16	68.8	4.7	134.8	9.2
0	Timna30-00	2	7	81	0.4	158.8	0.8

Table S6. Timna-30 group archaeointensity.

		Unmodeled Age (BCE)							Modeled Age (BCE)						
Sample	14C age	From (68.3%)	To (68.3%)	From (95.4%)	To (95.4%)	μ	median	σ	From (68.3%)	To (68.3%)	From (95.4%)	To (95.4%)	μ	median	σ
S1-w7	2859 ± 34	-1108	-937	-1184	-919	-1029	-1028	59	-1106	-1009	-1126	-939	-1050	-1046	45
S1-d3	2893 ± 39	-1155	-1009	-1213	-936	-1082	-1079	65	-1057	-985	-1095	-934	-1021	-1021	38
S1-g1	2819 ± 35	-1012	-922	-1109	-851	-974	-972	51	-1011	-944	-1040	-919	-977	-979	31
S2-g1	2814 ± 34	-1008	-923	-1103	-841	-968	-967	48	-967	-909	-1008	-895	-942	-940	30
S2-W1	2705 ± 35	-898	-812	-916	-804	-859	-857	34	-916	-828	-971	-807	-880	-884	36

Table S7. Timna-30 radiocarbon data.

Layer	From (68.3%)	To (68.3%)	From (95.4%)	To (95.4%)	μ	median	σ
0	-890	-788	-952	-763	-849	-856	39
1	-942	-868	-990	-851	-911	-912	33
2	-973	-914	-1013	-898	-947	-946	30
3	-986	-924	-1022	-905	-957	-957	30
4	-998	-934	-1031	-912	-967	-968	31
5	-1005	-939	-1035	-916	-972	-973	31
6	-1042	-971	-1077	-929	-1006	-1007	36
7	-1073	-993	-1105	-936	-1031	-1029	40
8	-1106	-1009	-1126	-939	-1050	-1046	45
9	-1139	-1025	-1147	-942	-1069	-1063	50

Table S8. Modeled radiocarbon ages of the slag layers in Timna-30 slag mound.

Group name	Age range	N fragments	n specimens	B (μT)	B σ (μT)	VADM (ZAm^2)	VADM σ (ZAm^2)
lmlk_old	-800, -701	4	12	73.8	9.5	141.2	18.1
Private_Stamp	-800, -701	3	11	72.6	4.3	138.9	8.2
lmlk_young[a]	-701, -630	7	24	69.7	5.3	133.2	10.1
Rosette	-660, -586	2	7	71.9	0.6	137.3	1.2
Lion[a]	-586, -520	3	11	65.8	2.1	125.7	4.1

Table S9. Archaeointensity group data of the Judean handles. Age ranges are slightly different than those in Ben-Yosef et al. (2017) and are based on Vaknin et al. (submitted).

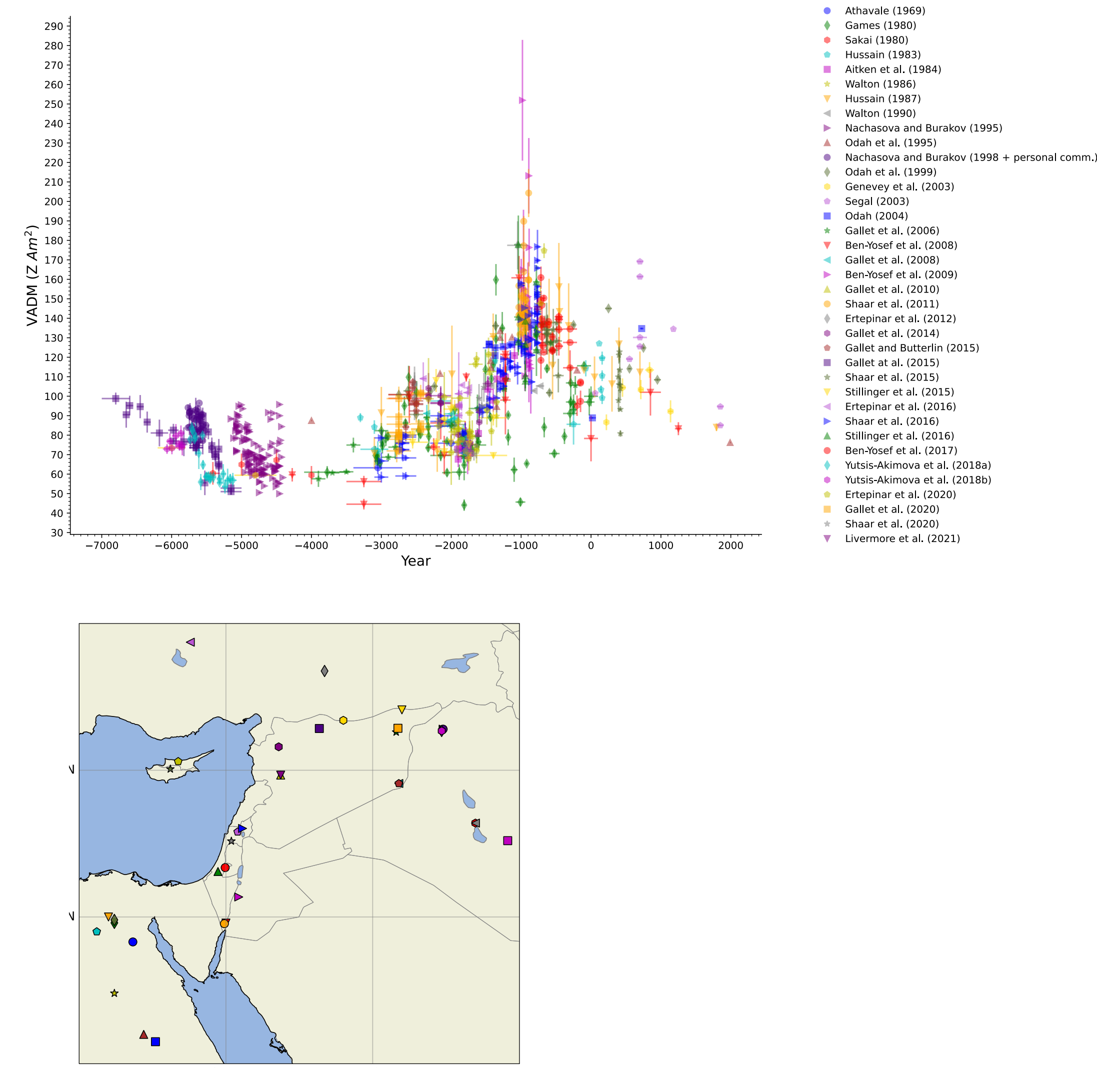

Figure S1: All archaeointensity data published from 1969-2021 in the locations shown on the map.

References

Ben-Yosef, E., Millman, M., Shaar, R., Tauxe, L., & Lipschits, O. (2017). Six centuries of geomagnetic intensity variations recorded by royal Judean stamped jar handles. *Proceedings of the National Academy of Sciences of the United States of America, 114*(9), 2160-2165 https://doi.org/10.1073/pnas.1615797114

Ben-Yosef, E., Tauxe, L., Levy, T. E., Shaar, R., Ron, H., & Najjar, M. (2009). Geomagnetic intensity spike recorded in high resolution slag deposit in Southern Jordan. *Earth and Planetary Science Letters, 287*(3-4), 529-539 https://doi.org/10.1016/j.epsl.2009.09.001

Gallet, Y., Fortin, M., Fournier, A., Le Goff, M., & Livermore, P. (2020). Analysis of geomagnetic field intensity variations in Mesopotamia during the third millennium BC with archeological implications. *Earth and Planetary Science Letters, 537* https://doi.org/10.1016/j.epsl.2020.116183

Gallet, Y., Genevey, A., Le Goff, M., Fluteau, F., & Ali Eshraghi, S. (2006). Possible impact of the Earth's magnetic field on the history of ancient civilizations. *Earth and Planetary Science Letters, 246*(1-2), 17-26 https://doi.org/10.1016/j.epsl.2006.04.001

Genevey, A. S., Gallet, Y., & Margueron, J. C. (2003). Eight thousand years of geomagnetic field intensity variations in the eastern Mediterranean. *Journal of Geophysical Research-Solid Earth, 108*(B5) https://doi.org/10.1029/2001jb001612

Lev, R., Bechar, S., & Boaretto, E. (2021). Hazor EB III city abandonment and IBA people return: radiocarbon chronology and its implications. *Radiocarbon, 63*(5), 1453-1469 https://doi.org/10.1017/RDC.2021.76

Levy, T. E., Higham, T., Ramsey, C. B., Smith, N. G., Ben-Yosef, E., Robinson, M., et al. (2008). High-precision radiocarbon dating and historical biblical archaeology in southern Jordan. *Proceedings of the National Academy of Sciences of the United States of America, 105*(43), 16460-16465 https://doi.org/10.1073/pnas.0804950105

Masetti-Rouault, M. G. (2016). Assyrian colonization in Eastern Syria: the case of Tell Masaikh (ancient Kar-Ashurnasirpal). In J. MacGinnis, D. Wicke, T. Greenfield, & A. Stone (Eds.), *The provincial archaeology of the Assyrian empire* (pp. 199-212): MacDonald institute monograph.

Reimer, P. J., Austin, W. E. N., Bard, E., Bayliss, A., Blackwell, P. G., Ramsey, C. B., et al. (2020). The Intcal20 Northern hemisphere radiocarbon age calibration curve (0-55 Cal Kbp). *Radiocarbon, 62*(4), 725-757 https://doi.org/10.1017/Rdc.2020.41

Shaar, R., Bechar, S., Finkelstein, I., Gallet, Y., Martin, M. A. S., Ebert, Y., et al. (2020). Synchronizing Geomagnetic Field Intensity Records in the Levant Between the 23rd and 15th Centuries BCE: Chronological and Methodological Implications. *Geochemistry Geophysics Geosystems, 21*(12) https://doi.org/10.1029/2020GC009251

Shaar, R., Ben-Yosef, E., Ron, H., Tauxe, L., Agnon, A., & Kessel, R. (2011). Geomagnetic field intensity: How high can it get? How fast can it change?

Constraints from Iron Age copper slag. *Earth and Planetary Science Letters, 301*(1-2), 297-306 https://doi.org/10.1016/j.epsl.2010.11.013

Shaar, R., Tauxe, L., Ron, H., Ebert, Y., Zuckerman, S., Finkelstein, I., & Agnon, A. (2016). Large geomagnetic field anomalies revealed in Bronze to Iron Age archeomagnetic data from Tel Megiddo and Tel Hazor, Israel. *Earth and Planetary Science Letters, 442*, 173-185 https://doi.org/10.1016/j.epsl.2016.02.038

Vaknin, Y., Shaar, R., Lipschits, O., Mazar, A., Maeir, A., Garfinkel, Y., et al. (in press). Reconstructing biblical military campaigns using geomagnetic field data *Proceedings of the National Academy of Sciences*